Title

Designing Yolk-Shell Nanostructures for Reversible Water-Vapor-Responsive Dual-Mode Switching of Fluorescence and Structural Color.

Permalink

https://escholarship.org/uc/item/9sc1w8bx

Authors

Zuo, Zhi-Han
Feng, Zi-Wen
Peng, Ying-Ying
et al.

Publication Date

2024

DOI

10.1021/acsnano.3c11092

Designing Yolk-Shell Nanostructures for Reversible Water-Vapor-Responsive Dual-Mode Switching of Fluorescence and Structural Color

Zhi-Han Zuo[a], *Zi-Wen Feng*[a], *Ying-Ying Peng*[a], *Yucong Su*[d], *Zhao-Qing Liu*[a], *Guogang Li*[b,c*], *Yadong Yin*[d], *and Yibo Chen*[a*]

[a] *School of Chemistry and Chemical Engineering/Institute of Clean Energy and Materials/Key Laboratory for Clean Energy and Materials, Guangzhou University, Guangzhou Higher Education Mega Center, No. 230 Wai Huan Xi Road, 510006, P. R. China*

[b] *Faculty of Materials Science and Chemistry, China University of Geosciences, Wuhan, Hubei 430074, P. R. China*

[c] *Zhejiang Institute, China University of Geosciences, Hangzhou, Zhejiang 311305, P. R. China*

[d] *Department of Chemistry, University of California Riverside, CA 92521, USA*

**Corresponding authors: Yibo Chen, E-mail: chenyibo@gzhu.edu.cn; Guogang Li, E-mail: ggli@cug.edu.cn.*

Abstract

Metal halide perovskites are offering ample opportunities to develop advanced optoelectronic devices. This work showcases that the integration of metal halide perovskites into metal oxide nanoshells with controllable interior cavities can enable water-vapor-responsive dual-mode switching of fluorescence and structural color. Through a ship-in-a-bottle method to introduce a controlled amount of $CsPbBr_3$ into MnO_2 nanoshells, we have designed $CsPbBr_3$@MnO_2 yolk-shell nanostructures, which can uptake a defined amount of water to exhibit rapid (less than 1 second) and reversible ($\geq$100 cycles) responses in both fluorescence on-off and color change when exposed to dynamic water vapor. These responses originate from the water-triggered phase transformation of $CsPbBr_3$ to $CsPb_2Br_5$ and the structural color change of the MnO_2 shell. The altered electronic and bonding structure at the oxide-halide interface, rapid water accumulation in the yolk-shell cavity, and protective effect of the oxide shell facilitate the reversible transformations. The response characteristics of the yolk-shell nanostructures have been further demonstrated in fabricating patterned films capable of multiple fluorescence/structural color responses, highlighting their potential for applications in advanced anti-counterfeiting and encryption.

Keywords: Metal halide perovskites, yolk-shell nanostructures, dual-mode responses, water vapor stimulation, hollow MnO_2 spheres

1. INTRODUCTION

In the last decade, metal halide perovskites (MHPs) have become promising materials in the optoelectronic field due to their versatile optoelectronic properties and low-cost solution processability.[1–3] On account of their ionic nature and low formation enthalpies, they are sensitive to external stimuli such as water, oxygen, light, and heat.[4–6] This sensitivity has initiated the development of responsive MHPs, including hydrochromic,[7–9] thermochromic,[10,11] photochromic,[12,13] and mechanochromic ones.[14] Among them, water-stimulated MHPs fluorescence switches are deemed as most encouraging due to the low cost and environmental friendliness of the stimulus, as well as their application potential in areas such as anti-counterfeiting, information encryption/decryption, and humidity sensing.[15–18] However, the intrinsic instability of MHPs always leads to irreversible degradation of the crystal framework when they are exposed to water. This poses a significant challenge in achieving reversibly switchable water-responsive fluorescence in MHPs. In addition, a single fluorescent switching mode is unable to meet the requirements for advanced anti-counterfeiting or information encryption in terms of optical signal complexity. Therefore, constructing composite structures based on MHPs to achieve highly reversible and multi-mode hydrochromic performance is extremely crucial for advanced anti-counterfeiting applications.

Several works have been conducted, with a particular focus on enhancing the stability of the metal halides during water treatment.[19–22] For example, Yu et al. capsulated $CsPbBr_3$ nanocrystals into mesoporous silica nanospheres to achieve a reversible transformation between luminescent $CsPbBr_3$ and non-luminescent $CsPb_2Br_5$ upon exposure to or removal of water.[19] Zhang et al. developed water-resistant nanocrystals by confining $Cs_3Cu_2I_5$ within a polymer shell. These water-resistant nanocrystals were combined with bare $Cs_3Cu_2I_5$ to assemble sophisticated anti-counterfeiting patterns relying on the water-induced structure transformation between blue-emitting $Cs_3Cu_2I_5$ and yellow-emitting $CsCu_2I_3$.[20] However, the reported response performance of MHPs is still considered unsatisfactory. Few studies have reported the repetition of these water-responsive processes beyond 20 times. Furthermore, composite systems that exhibit more than two types of water-responsive optical properties are exceptionally rare.

Mono-dispersed hollow manganese dioxide (*h*-MnO_2) nanospheres, very recently reported by us as a hydrochromic candidate,[23] provide an opportunity to address the above challenges. These nanospheres possess three key features that contribute to their effectiveness. First, they introduce a water-responsive structural color to the composite system. Additionally, the nanoscale porosity formed in the MnO_2 shells enhances the capillary condensation of dynamic water vapor and facilitates rapid water accumulation within the cavity. Further, this cavity can serve as both a water reservoir and a protective reaction chamber for the structural transformation of the MHPs. Herein, we encapsulated $CsPbBr_3$ nanocrystals into hollow MnO_2 spheres to construct a $CsPbBr_3$@MnO_2 yolk-shell nanostructure, in which the cavity size can be tailored by simply tuning the concentration of the precursors. The $CsPbBr_3$@MnO_2 yolk-shell structure with a moderate-size cavity shows highly reversible ($\geq$100 cycles) and rapid (less than one second) fluorescence/structural color dual-mode switching when stimulated by dynamic water vapor. In contrast, it does not show any response to static water vapor or trace water. Through in-depth experimental plus theoretical investigations, the dual-mode response mechanism has been revealed. Considering the multiple responses of $CsPbBr_3$@MnO_2 yolk-shell nanostructure, we further demonstrate its application feasibility on optical anti-counterfeiting and encryption/decryption.

2. RESULTS AND DISCUSSION

Construction of Yolk-Shell Nanostructure. The $CsPbBr_3@MnO_2$ yolk-shell structure was constructed by an amino-assisted ship-in-a-bottle method (**Figure 1**a, see Supporting information file for details). The hollow MnO_2 nanospheres (*h*-MnO_2) were prepared first by a facile surface-initiated redox method with silica spheres as the hard template, and then the prepared *h*-MnO_2 were modified with (3-Aminopropyl) triethoxysilane (APTES). Note here that the modified *h*-MnO_2 should be thoroughly washed with ethanol to stripe the surplus amino groups. Within an anti-solvent precipitation process, the $CsPbBr_3$ nanocrystals can be located in the *h*-MnO_2 cavity and the growth mechanism is discussed as follows.

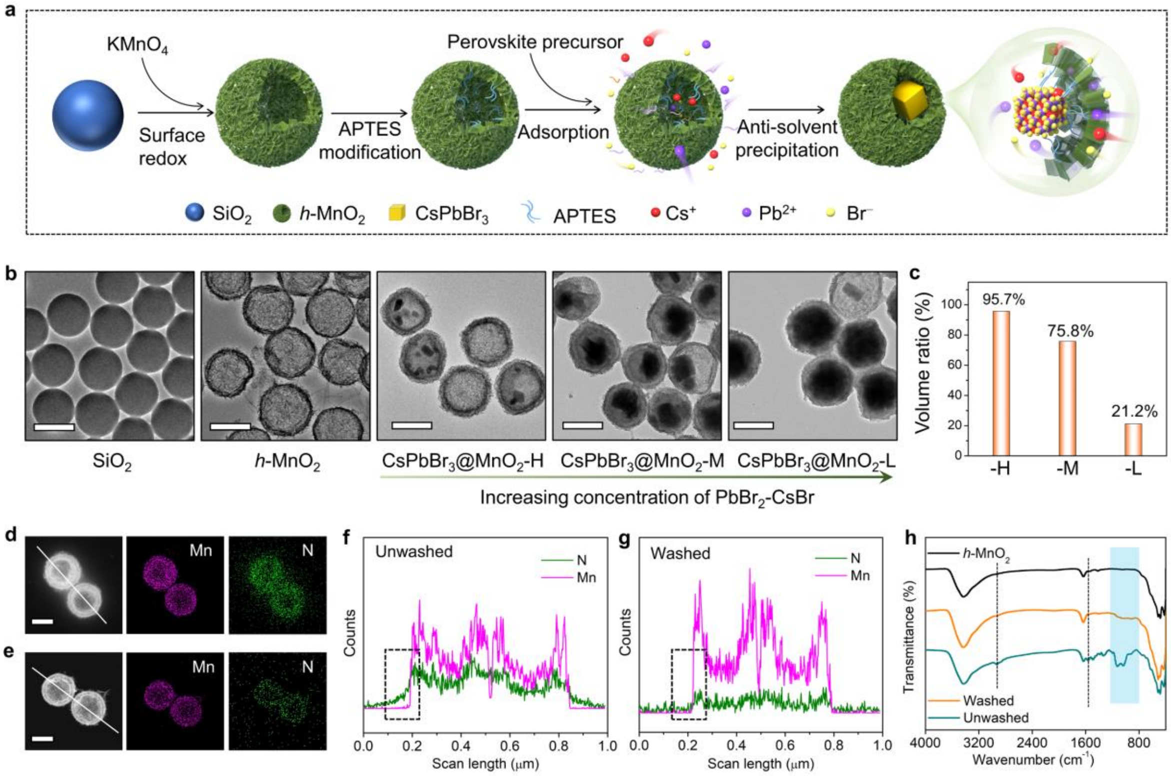

Figure 1. Construction of yolk-shell $CsPbBr_3@MnO_2$ nanostructures. (a) Synthesis scheme. (b) TEM images of SiO_2 spheres, *h*-MnO_2, and $CsPbBr_3@MnO_2$ samples made with $PbBr_2$-CsBr concentration at 0.015, 0.035, and 0.055 mmol/mL for -H, -M, and -L. (c) Cavity volume ratios in -H, -M, and -L samples. (d-h) Comparison of surface functional groups in unwashed and washed *h*-MnO_2 after modification of APTES. Elemental mapping images of unwashed (d) and washed (e) *h*-MnO_2. Linear scanning spectra of unwashed (f) and washed (g) *h*-MnO_2. (h) FTIR spectra. Scale bars in all TEM images are 200 nm.

The transmission electron microscope (TEM) images of the structures prepared with different concentrations of $PbBr_2$-CsBr precursor are shown in Figure 1b. When the concentration of $PbBr_2$-CsBr increases from 0.015 to 0.055 mmol/mL, the $CsPbBr_3$ core in the MnO_2 shell gradually grows to a bigger size until fills the whole cavity. A yolk-shell $CsPbBr_3$@MnO_2 structure is obtained with the optimized $PbBr_2$-CsBr concentration at 0.035 mmol/mL. Further increasing the $PbBr_2$-CsBr concentration to 0.070 mmol/mL enables the growth of $CsPbBr_3$ both on the inner and outer surface of the shell (Figure S1). The volume ratios of the cavity (r_c) in the samples prepared with 0.015, 0.035, and 0.055 mmol/mL $PbBr_2$-CsBr precursors are roughly calculated with the formula $r_c = p_{\mathrm{Nucleation}} \cdot r_{\mathrm{cavity}}$, where $p_{\mathrm{Nucleation}}$ is the probability of nucleation, i.e., the number of the MnO_2 hollow spheres filled by MHPs among all the spheres, and r_{cavity} refers to the volume ratio of the cavity in one filled MnO_2 hollow sphere. The results demonstrate a decreasing trend in the volume ratio of the cavity with an increasing concentration of $PbBr_2$-CsBr (Figure 1c). Thus, we named the typical samples prepared with 0.015, 0.035, and 0.055 mmol/mL $PbBr_2$-CsBr precursors $CsPbBr_3$@MnO_2-H, -M, -L, where “H”, “M”, and “L” refer to the cavity ratio as high, medium, and low, respectively.

To verify the growth mechanism of the yolk-shell structure, a series of control experiments were conducted. Without a prior modification of the amino group, $CsPbBr_3$ nanocrystals cannot be encapsulated into the *h*-MnO_2 spheres (Figure S2). Moreover, when the *h*-MnO_2 is not thoroughly washed after modification, $CsPbBr_3$ nanocrystals tend to grow both on the outer and inner surfaces of the *h*-MnO_2 nanospheres (Figure S3). To clarify the washing effect, we compare the elemental mapping images and Fourier transform infrared (FTIR) spectra of the APTES-modified *h*-MnO_2 with or without washing procedure. The unwashed *h*-MnO_2 is capped by a lot of amino groups on both the inner and outer surfaces, which can be seen by the mapping images and linear scanning spectra of elements N and Mn (Figure 1d and Figure 1f). After washing the modified *h*-MnO_2 with ethanol twice, the range of N is limited to the inner surface (Figure 1e and Figure 1g). In addition, the characteristic FTIR bands of the functional groups in APTES decrease after washing, including N-H bending vibration at 1560 cm^{-1}, $-CH_2$ at 2935 cm^{-1}, and Si-O at 1123 and 1035 cm^{-1} (Figure 1h).[24,25] The above comparison indicates that the amino groups on the outer surface tend to be lost during the wash process while the inner ones can be maintained, primarily due to the limited mobility of the APTES molecules within the spherical shell. The amino groups on the inner surface preferably catch Br^{-} so that the $CsPbBr_3$ nanocrystals can be anchored into the *h*-MnO_2 nanospheres.[26,27] Once the $CsPbBr_3$ nanocrystals are precipitated on the inner surface of the *h*-MnO_2, the concentration gradient resulting from the decreased ion concentration inside the spherical shell further promotes the penetration of ions into the interior of the sphere, ultimately leading to the formation of a $CsPbBr_3$ nanocrystal within the MnO_2 shell. Therefore, precise modification of the amino groups on the inner surface of the *h*-MnO_2 spheres is crucial for the construction of yolk-shell $CsPbBr_3$@MnO_2 nanostructures.

The chemical compositions of the $CsPbBr_3$@MnO_2 samples are identified by X-ray diffraction (XRD) measurement (Figure S4). The high-resolution TEM image of the $CsPbBr_3$@MnO_2-M composite displays the close contact between MnO_2 and $CsPbBr_3$. The *d* spacing value is derived to be 0.338 nm, corresponding to the (111) plane of the $CsPbBr_3$ lattice (**Figure 2**a-c). The elemental mapping images confirm that Cs, Pb, and Br elements are distributed in the center, while Mn and O elements are distributed around to form a shell layer (Figure 2d). The X-ray photoelectron spectroscopy (XPS) spectra of the single-phase and the composite samples are shown in Figure 2e, f, and Figure S5. The Br $3d_{3/2}$ and Br $3d_{5/2}$ peaks of the $CsPbBr_3$ nanocrystals are located at 67.83 and 68.85 eV.[28,29] In $CsPbBr_3$@MnO_2-M, the binding energy of Br $3d_{5/2}$ shifts 0.24 eV towards a higher value compared to that in the $CsPbBr_3$ nanocrystals. In the Mn $2p_{3/2}$ spectrum of *h*-MnO_2, the peaks at 641.26/652.66, 642.33/653.92, and 643.86/654.88 eV correspond to Mn(II), Mn(III), and Mn(IV), respectively.[30,31] After integrating with $CsPbBr_3$, the *h*-MnO_2 shows an increased proportion of Mn(II), suggesting a reduction in the valence state of Mn. The above XPS results establish the occurrence of electronic interactions between Mn and Br atoms at the $CsPbBr_3$/MnO_2 interface, wherein Mn loses electrons and Br gains them. The Raman band at 639 cm^{-1} is attributed to the symmetric stretching vibration of the Mn-O bond in $[MnO_6]$ octahedron.[32] The band becomes wider in $CsPbBr_3$@MnO_2-M (Figure 2g), mainly due to the enhanced lattice distortion of the *h*-MnO_2 after integrating with $CsPbBr_3$. The above results confirm the electronic interactions between $CsPbBr_3$ and MnO_2.

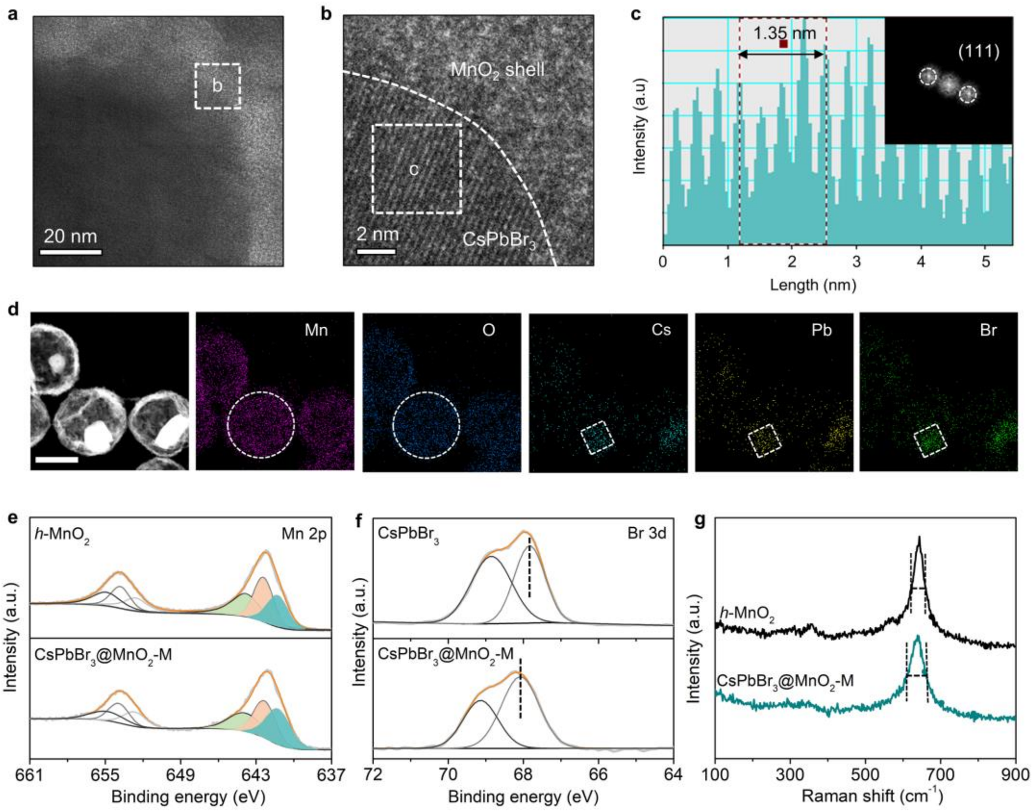

Figure 2. Microstructure of $CsPbBr_3$@MnO_2-M. (a) TEM image and (b) high-resolution TEM image of the magnified heterointerface between MnO_2 and $CsPbBr_3$. (c) The *d* spacing value and Fourier Transform pattern (inset) of the corresponding plane in (c). (d) Elemental mapping images. The scale bar is 200 nm. XPS spectra of (e) Mn 2p and (f) Br 3d. (g) Raman spectra.

Cavity-Dependent Reversible Fluorescence/Structural Color Switching. The optical response performance was investigated after the $CsPbBr_3$@MnO_2-H, -M, -L nanospheres were randomly assembled to be films with a thickness of ~1.5 μm (**Figure 3**a and Figure S6). The responses of the $CsPbBr_3$@MnO_2-H, -M, -L films in fluorescence (under UV light) and structural color (under natural light) when exposed to dynamic water vapor are visualized in Figure 3b. The time-resolved fluorescence and reflectance spectra of the films were recorded using a homemade device setup (Figure 3c). Real-time monitoring and control of the relative humidity (RH) and flow rate (*r*) of the water vapor were achieved using a humidity meter, a flow meter, and various supersaturated salt solutions.

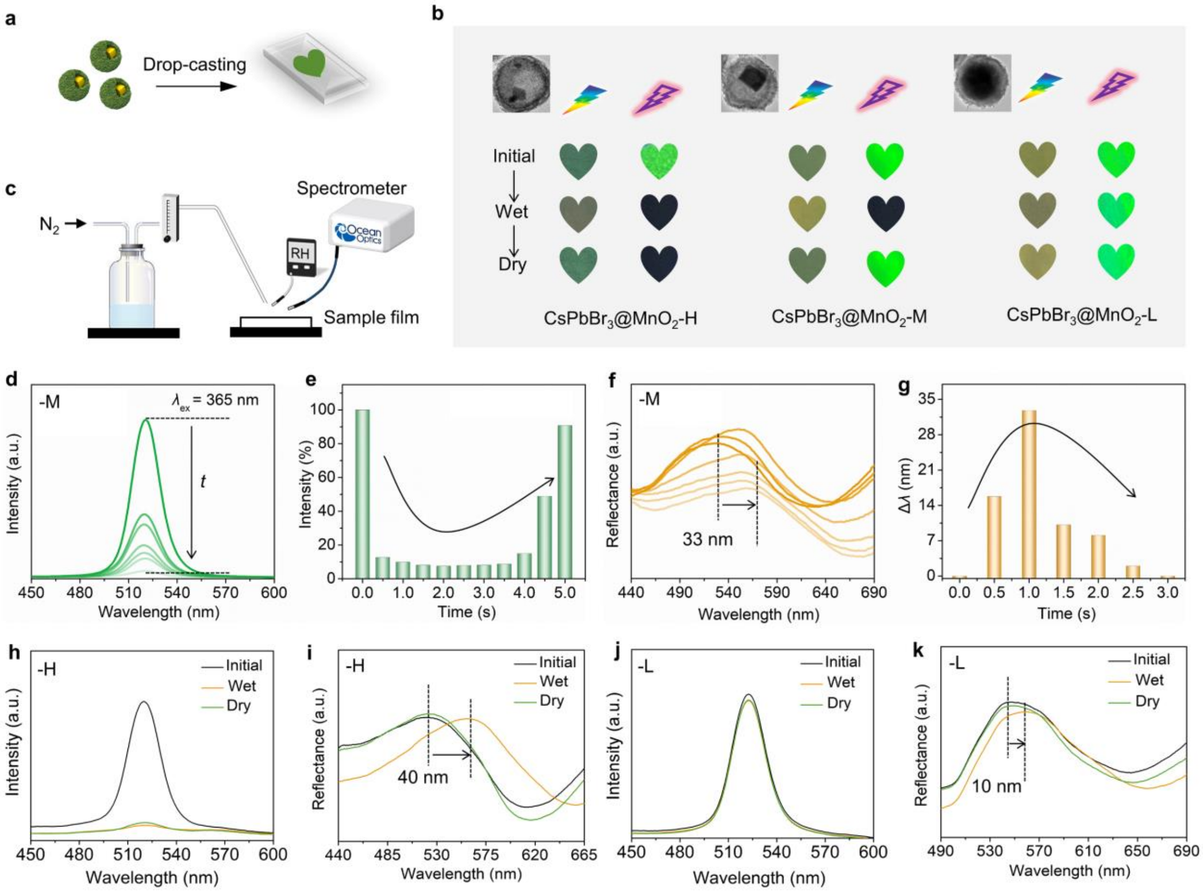

Figure 3. Dual-mode response triggered by water vapor with relative humidity (RH) of 100% and flow rate (*r*) of 6 L/min. (a) Assembly of the film. (b) Corresponding digital images of the films upon exposure to high-humidity dynamic water vapor. (c) Measurement device set. Time-dependent (d) fluorescence spectra, (e) fluorescence intensity, (f) reflectance spectra, and (g) reflectance wavelength of $CsPbBr_3@MnO_2$-M film. The time interval of each line in Figure 3d and Figure 3f is 100 milliseconds. (h) Fluorescence and (i) reflectance spectra of $CsPbBr_3@MnO_2$-H film. (j) Fluorescence and (k) reflectance spectra of $CsPbBr_3@MnO_2$-L film.

The films initially exhibit a green color under natural light. The color here is the structural color of MnO_2 hollow spheres, which is a coloration generated by the interaction of light with micro- and nanostructures, with advantages such as long-term stability, low toxicity, low device dependence, and environmental friendliness.[33–35] At the same time, the films emit a green fluorescence under a 365 nm excitation, originating from the $CsPbBr_3$ nanocrystals. Upon exposure to water vapor at 100% RH and a flow rate of 6 L/min, the $CsPbBr_3@MnO_2$-M film demonstrates a significant decrease in fluorescence intensity, with the peak located at 520 nm dropping to 8.7% of the initial value within approximately 600 milliseconds (Figure 3d). After the vapor is removed, the fluorescence gradually recovers over a period of about four seconds (Figure 3e). The reflectance spectra, as shown in Figure 3f, initially peak at 529 nm and then undergo a redshift of 33 nm to 562 nm in less than one second upon stimulation of water vapor. After three seconds, the film color also recovers, as depicted in Figure 3g. The rapid and reversible process can be observed in Video S1. The $CsPbBr_3$@MnO_2-H film exhibits a sharp decline in fluorescence upon exposure to dynamic water vapor, but this fluorescence cannot be reproduced after evaporation of water (Figure 3h). Initially, the reflectance peak of the $CsPbBr_3$@MnO_2-H film is located at 520 nm. When exposed to dynamic water vapor, the peak undergoes a redshift of 40 nm, which is larger than that observed for $CsPbBr_3$@MnO_2-M (33 nm) (Figure 3i). The fluorescence spectra of $CsPbBr_3$@MnO_2-L under dynamic water vapor are almost the same in the whole stimulation process (Figure 3j). The reflectance peak of the $CsPbBr_3$@MnO_2-L film is initially located at 555 nm and only shows a redshift of 10 nm upon dynamic water vapor (Figure 3k). The shifting difference of the reflectance spectra in the three structures will be discussed in the following mechanism section. Based on the above comparisons, appropriate cavity volume in the $CsPbBr_3$@MnO_2 nanostructure is proved to be an important factor for the reversible dual-mode responses.

The response performance of the $CsPbBr_3$@MnO_2-M film towards water vapor with different RH and flow rates was investigated. The results show that the film has a higher response sensitivity to high-humidity water vapor compared to low-humidity ones (Figure S7). When the humidity level drops to 70%, only a minor fluorescence decline can be observed even when the time is extended to 30 seconds. The fluorescence variation trend remains almost consistent under water vapor with 100% RH at flow rates of 3~9 L/min (Figure S8). In contrast, when the water vapor flow rate is 0, the film shows no response (Figure S9). The trace water detection measurement was also performed, and it shows that the fluorescence of the $CsPbBr_3@MnO_2$-M nanospheres remains unquenched until the water concentration increases to approximately 1.0% in tetrahydrofuran (THF) solution (Figure S10). This finding suggests that the nanospheres are not responsive to trace amount of water and are therefore unsuitable for trace water measurement, in contrast to the previous reports.[7,36,37] In addition, blue-emitting $CsPbBr_{3-x}Cl_x@MnO_2$-M could be obtained by simply replacing CsBr with CsCl in the perovskite precursors, and it also exhibits dual-mode reversible color-changing properties in response to dynamic water vapor (Figure S11). The above results demonstrate that only the "dynamic" water vapor with a certain flow rate and high humility (≥80%) can trigger the response of the $CsPbBr_3@MnO_2$-M film, highlighting its response selectivity and the application potential in fields of anti-counterfeiting and encryption.

Water-Stimulated Phase Transformation in the Composite. To monitor the water-stimulated phase transformation, time-dependent XRD patterns of the $CsPbBr_3@MnO_2$-M nanospheres were recorded after water droplets were applied, and the bare $CsPbBr_3$ nanocrystals were also measured for comparison. Because the film is too thin to record the XRD patterns, powder samples were used to monitor the water-induced structure evolution. Thus, the time consumption here is longer than that for the films. The XRD peaks of $CsPbBr_3$ in $CsPbBr_3@MnO_2$-M nanospheres disappear after 10 minutes, while the peaks at 29.3°, 33.3°, and 47.6° are presenting, corresponding to the (213), (310), and (413) crystal planes of $CsPb_2Br_5$.[38] After 20 minutes, the $CsPbBr_3$ phase reappear along with $CsPb_2Br_5$ and ultimately become the main phase after 30 minutes (**Figure 4**a). However, the $CsPbBr_3$ nanocrystals (The TEM image is shown in Figure S12) still maintain the initial phase after 30 minutes of water erosion, with only one weak diffraction peak appearing at 29.3° corresponding to the (213) crystal plane of $CsPb_2Br_5$ (Figure 4b). Accordingly, the fluorescence intensity of the $CsPbBr_3$ nanocrystals is quite stable under the stimulation of water vapor (Figure 4c). These results demonstrate the water-induced phase transformation between $CsPbBr_3$ and $CsPb_2Br_5$ in the composite system and prove that the $CsPbBr_3$ adhered to MnO_2 is more sensitive to water than bare $CsPbBr_3$.

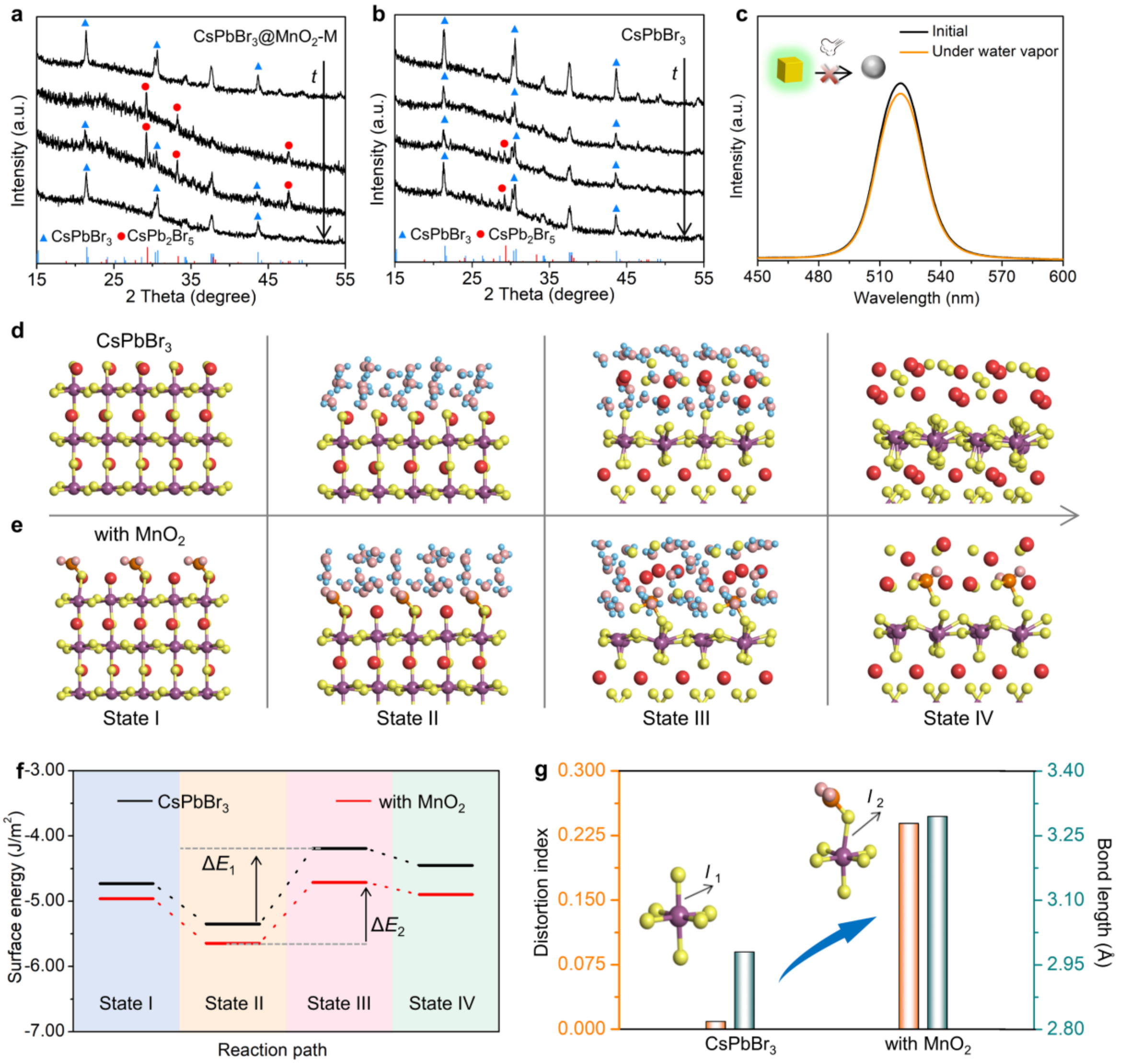

Figure 4. Accelerated phase transformation of metal halides in the composite. Time-dependent XRD patterns of (a) $CsPbBr_3@MnO_2$-M and (b) $CsPbBr_3$ under water stimulation. (c) Fluorescence spectra of bare $CsPbBr_3$ under dynamic water vapor. Simulated reaction steps of (d) $CsPbBr_3$ and (e) $CsPbBr_3$ combined with MnO_2 under a certain amount of water. (The red, purple, yellow, orange, blue, and pink balls represent Cs, Pb, Br, Mn, H, and O atoms, respectively). (f) Surface energy

values during the reaction process. (g) Distortion index and bond length of a specified [$PbBr_6$] with or without bonding to MnO_2.

To clarify the accelerated phase transformation in the composite system, the structure evolution steps and surface energy of $CsPbBr_3$ under water stimulation were theoretically simulated and calculated, both with or without MnO_2. The evolution process is divided into four stages, with State I-IV referring to the initial state (I), the state after adsorption of water molecules (II), the state of $CsPbBr_3$ has been transformed into $CsPb_2Br_5$ by stripping of CsBr (III), and the state of CsBr and $CsPb_2Br_5$ after evaporation of water (IV), respectively (Figure 4d and Figure 4e). The surface energy values of each state in the two pathways are diagramed in Figure 4f. The process from state II to state III is determined to be the key step because only this step shows an energy barrier to be overcome. For bare $CsPbBr_3$, an energy barrier of 1.16 J/m^2 (ΔE_1) needs to be overcome for stripping CsBr and further initiating the structural transformation to $CsPb_2Br_5$. Whereas for the composite system of $CsPbBr_3/MnO_2$, the energy barrier is lower ($\Delta E_2 = 0.94$ J/m^2), allowing the reaction to proceed more easily. A typical [$PbBr_6$] octahedron in State II with or without bonding with MnO_2 is magnified in Figure 4g and the bonding parameters are shown in Table S1. The octahedron bonding with MnO_2 shows a longer Pb-Br bond length (l_2 = 3.295 Å) and a higher lattice distortion index (D_2 = 0.239) compared with the isolated [$PbBr_6$] octahedron (l_1 = 2.980 Å, D_1 = 0.009). This is consistent with the Raman results, that the lattice distortion has been enlarged in the composite. The above results prove that the electronic interactions at the heterointerfaces between MnO_2 and $CsPbBr_3$ can alter the localized structure and make the Pb-Br bond more likely to be broken, thus promoting the structural transformation rate.

Based on the above experimental and theoretical results, the dual-mode response mechanism is illustrated in **Figure 5**a. In our previous work,[23] we have demonstrated that water vapor tends to condense and create droplets within the mesopores formed by the stacking of MnO_2 nanosheets (The pore size distribution of the $CsPbBr_3$@MnO_2-M nanospheres is shown in Figure S13). This condensation process, known as capillary condensation, occurs due to the Laplace pressure (ΔP) generated by the concave water meniscus within the pores.[39–41] Further, the vapor flow at a certain rate helps to squeeze the air in the cavity, accelerating water condensation within it. Due to the higher refractive index of water ($n_{\mathrm{water}} = 1.33$) than air ($n_{\mathrm{air}} = 1.0$), the reflectance wavelength of the composite system shows a redshift according to Bragg equation $\lambda = 2dn\ sin\ \theta$,[42] where d is the spacing between the (crystal) planes, n is the effective refractive index of the system, and θ is the viewing angle. At the same time, once water starts to accumulate in the cavity, the phase transformation of $CsPbBr_3$ nanocrystals to $CsPb_2Br_5$ will be triggered at the heterointerfaces between $CsPbBr_3$ and MnO_2, resulting in the fluorescence quenching of $CsPbBr_3$. After evaporation of water, both the phase and the fluorescence of $CsPbBr_3$ nanocrystals are restored. Herein, the capillary condensation of water vapor in h-MnO_2 and the subsequent water-stimulated phase transformation of $CsPbBr_3$ synergistically enables the dual-mode optical responses in structural color and fluorescence.

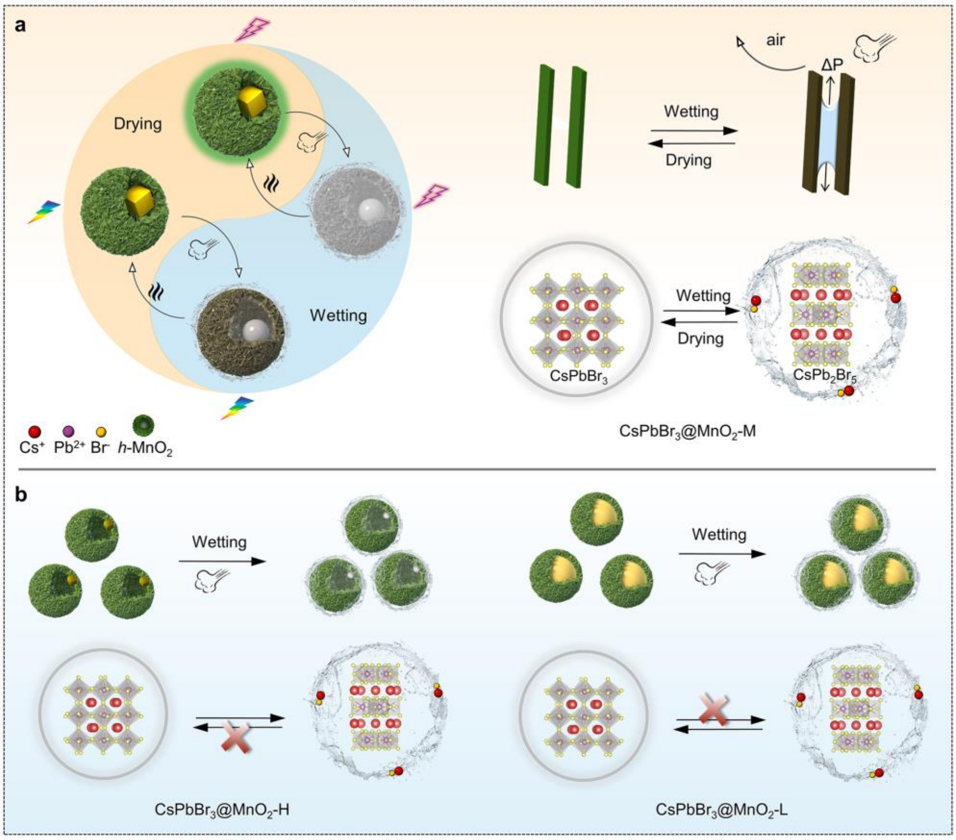

Figure 5. Schematic fluorescence/structural color synergistic switching mechanism. (a) Dual-mode response under stimulation of dynamic water vapor. (b) Cavity-dependent response process. (The red, purple, and yellow balls represent Cs, Pb, and Br atoms, respectively).

The comparison of the reflectance wavelength redshift among the three different structures (40, 33, and 10 nm for $CsPbBr_3@MnO_2$-H, -M, and -L, respectively) indicates a proportional relationship between the redshift and the volume ratio of the cavity. Because a larger redshift in the reflectance corresponds to a higher increase in the effective refractive index of the system, it can be inferred that an increase in the cavity volume allows for a larger amount of water to enter the cavity. Herein, the cavity-dependent response mechanism is illustrated in Figure 5b. For $CsPbBr_3@MnO_2$-H with a larger water-storage space, too much water makes the stripped Cs^+ and Br^+ over-dispersed and inevitably lost, thus the fluorescence is irreversible. On the other hand, the $CsPbBr_3@MnO_2$-L structure with the cavity space mostly occupied by the $CsPbBr_3$ core cannot store enough water to trigger the response. Only when there is an appropriate cavity volume in the yolk-shell system can a moderate amount of water be accumulated to trigger the reversible phase transformation and fluorescence transition of $CsPbBr_3$ nanocrystals.

Applications on Optical Anti-Counterfeiting and Encryption. Durability is an important criterion of responsive materials for practical applications. As shown in **Figure 6**a, both the fluorescence intensity and the reflectance peak wavelength of the yolk-shell $CsPbBr_3$@MnO_2-M film display reversible switches of the same magnitude during 100 cycles of dynamic water vapor stimulation. The fluorescence and reflectance spectra both keep the same peak value as the initial state at the end of each cycle. Meanwhile, the yolk-shell morphology and the XRD peaks of $CsPbBr_3$ are well maintained after 100 cycles (Figure S14 and Figure S15). The $CsPbBr_3$@MnO_2-M film which has been stored in air for 6 months still exhibits a reversible fluorescence quenching-recovery performance in a wetting-drying cycle, further confirming the stability of the composites (Figure S16). Compared with the previously reported water/moisture-responsive metal halides, the $CsPbBr_3$@MnO_2-M film shows more specified stimulus, dual-mode response in fluorescence and structural color, and record-high durability (Table S2),[7,9,16,19,20,22,36,43] demonstrating its application potential on high-level optical anti-counterfeiting and encryption.

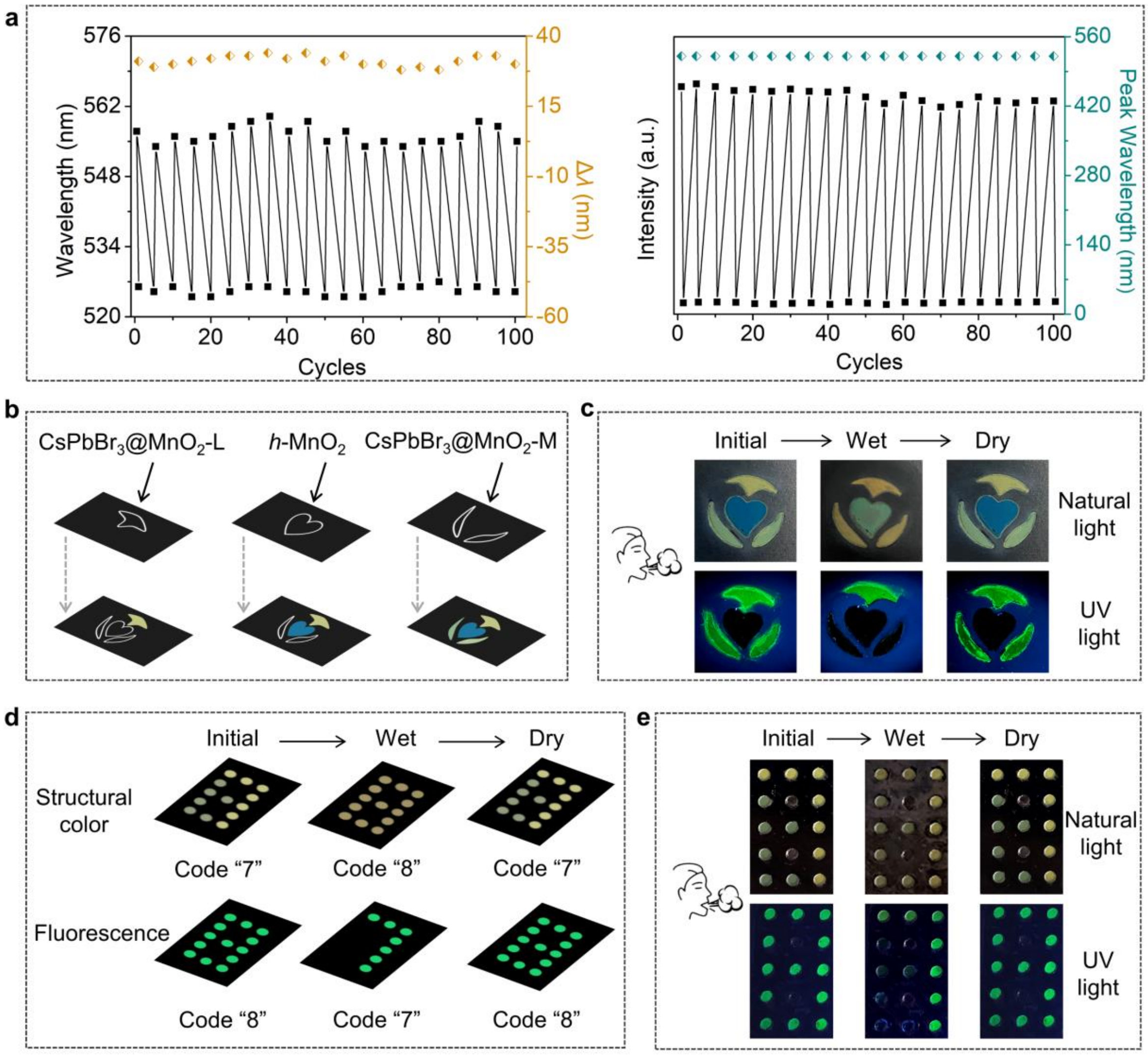

Figure 6. Applications in optical anti-counterfeiting and encryption. (a) Reversibility of the optical response in reflectance (left) and fluorescence (right) after 100 cycles of dynamic water vapor treatment. (b) Preparation process and (c) digital images of the dual-mode anti-counterfeiting patterns. (d) Schematic design principles and (e) corresponding digital images of the optical information encryption between code "7" and "8".

To evaluate the applicability of the prepared nanostructures, a dual-mode patterned anti-counterfeiting model was fabricated (Figure 6b). The human breath of an average adult with high RH (≈100%) and moderate flow rate (5-7 L/min) is an accessible stimulation source for the models. Under natural light, the model exhibits structural color signals including blue (filled by h-$\mathrm{MnO_2}$), green (filled by $\mathrm{CsPbBr_3@MnO_2}$-M), and yellow-green (filled by

$CsPbBr_3$@MnO_2-L). When stimulated by human breath, the pattern shows a redshift of the colors and recovers to the initial state after water evaporation. Whereas, a different fluorescence pattern can be seen under the excitation of a commercial 365 nm UV lamp, that only the parts filled by $CsPbBr_3$@MnO_2-M and $CsPbBr_3$@MnO_2-L emit green fluorescence. Upon human breath, the fluorescence of $CsPbBr_3$@MnO_2-M is quenched, while the fluorescence survives in $CsPbBr_3$@MnO_2-L. The fluorescence pattern also recovers in several seconds after water evaporation (Figure 6c). An arrayed model was further fabricated to imply more specific information. The $CsPbBr_3$@MnO_2-L nanospheres were filled into the “7” dots, and $CsPbBr_3$@MnO_2-M nanospheres were filled into the remaining dots to form a number “8” pattern (Figure 6d and Figure S17). When observing under natural light, one can see the yellow-green structural color code of “7”. It becomes indistinguishable under the stimulation of human breath and changes to code “8”, because the structural colors of $CsPbBr_3$@MnO_2-L and -M both shift towards longer wavelengths and eventually appear as similar yellow-green colors. After evaporation of water, it returns to code “7”. The fluorescence signal also presents a switch between codes “7” and “8”, but in a different sequence with the structural color signal. The initial state gives a fluorescence code of “8”. The code changes to “7” under the stimulation of human breath due to different responses of $CsPbBr_3$@MnO_2-M and -L. Ultimately, the code “8” appears again after the water vapor is removed (Figure 6e). The different response behaviors in structural color and fluorescence modes provide more complexity and reveal high application potentials in the fields of optical anti-counterfeiting, encryption/decryption, respiratory monitoring sensors, etc.

3. CONCLUSION

In summary, we showcase the integration of inorganic perovskite into oxide nanoshells to enable fluorescence/structural-color dual-mode responses that are highly sensitive to water vapor with moderate flow rates. Specifically, under water vapor with humidity at 100% and a flow rate at 6 L/min, the structural color of a film composed of $CsPbBr_3$@MnO_2 yolk-shell nanospheres transforms from green to yellow-green in a bright field, accompanied by simultaneous green fluorescence switching from “on” to “off” in a dark field. Such dual-mode color-switching originates from the water-triggered phase transformation of $CsPbBr_3$ to $CsPb_2Br_5$ and the structural color change of the MnO_2 shell. The rapidity (≈600 ms) and reversibility (more than 100 cycles) of the response are attributed to the electronic and bonding structure alteration at the interface between $CsPbBr_3$ and MnO_2, accelerated water accumulation in the yolk-shell cavity, as well as the confinement effect of the MnO_2 shell. Furthermore, incorporating $CsPbBr_3$@MnO_2 yolk-shell nanostructures into patterned films enables multiple responses, demonstrating the potential of the composites for applications such as anti-counterfeiting, optical information encryption/decryption, and sensing.

4. EXPERIMENTAL SECTION

Materials. All the raw chemical reagents were purchased and used directly without further purification. Tetraethyl orthosilicate (TEOS, AR), formaldehyde solution (AR), potassium permanganate ($KMnO_4$, AR), ammonia solution (AR, 25%), toluene (HPLC), and sodium hydroxide (NaOH, AR) were obtained from Guangzhou Chemicals. Resorcinol (AR, 99%), polyvinyl pyrrolidone (PVP, Mw = 10 000), (3-Aminopropyl) triethoxysilane (APTES, AR), N, N-dimethylformamide (DMF, 99.9%), hexane (99%), lead(II) bromide ($PbBr_2$, 99%), cesium bromide (CsBr, 99.9%), oleic acid (OA, A.R.), oleylamine (OAm, 80%-90%) were purchased from Shanghai Aladdin Chemicals. Ethanol was purchased from Tianjin Fuyu Fine Chemical Co., Ltd.

Synthesis of Hollow MnO_2 Nanospheres. The hollow MnO_2 (*h*-MnO_2) nanospheres were synthesized through a surface redox process.[23] Typically, 10.0 mL TEOS was mixed with 210.0 mL ethanol, 20.0 mL water, and 8.0 mL ammonia solution. By stirring the mixture at room temperature for four hours, SiO_2 nanospheres with a diameter of 200 nm were obtained. Next, 50.0 mg PVP-modified SiO_2 spheres, 28.0 mL water, 20.0 mg resorcinol, 28 μL formaldehyde solution, and 100 μL 2.8% newly-prepared ammonia solution were added into a three-neck flask. The reaction system was heated at 60 °C for two hours and then kept at 100 °C for another two hours. The obtained SiO_2@RF was mixed with 80 mg $KMnO_4$ to obtain SiO_2@MnO_2. After etched by 0.6 mol/L NaOH solution at 70 °C for three hours, the *h*-MnO_2 nanospheres were obtained.

Synthesis of $CsPbBr_3$@MnO_2 Composites. The amino-modified *h*-MnO_2 nanospheres were obtained by mixing the above *h*-MnO_2 nanospheres with 60.0 mL ethanol and 6.0 mL APTES for 12 hours, then the modified nanospheres were washed twice with ethanol and dispersed in 5.0 mL DMF. After that, 2.5 mL of the above dispersion, 250 μL of OA, 20 μL of OAm, and a specific quantity of $PbBr_2$ and CsBr were mixed and diluted to 5.0 mL with DMF before being stirred for 10 minutes. Then, 1.0 mL of the above precursor solution was quickly injected into 10.0 mL toluene and the mixture was consecutively stirred for two minutes. The sediment was collected by centrifugation and further washed with hexane three times. Because the adding ratio of $PbBr_2$ to CsBr is maintained to be 5:4 in mole, the concentration of $PbBr_2$ was designated to imply the concentration of $PbBr_2$-CsBr precursor. When the concentration of $PbBr_2$-CsBr precursor was 0.015, 0.035, and 0.055 mmol/mL, the final products were named

$CsPbBr_3$@MnO_2-H, -M, and -L, respectively. The $CsPbBr_{3-x}Cl_x$@MnO_2 composite was prepared with the same procedures except for replacing CsBr with CsCl. The $CsPbBr_3$ nanocrystals were obtained with the same protocol of $CsPbBr_3$@MnO_2-M but without the addition of *h*-MnO_2.

Preparation of Anti-Counterfeiting and Encryption Patterns. The responsive films were made by a drop-casting process. A $CsPbBr_3$@MnO_2 or other sample suspension (~5 mg/mL in hexane) was carefully dropped onto a hollow painting template and then heated in the oven to evaporate the solvent.

Characterizations. X-ray powder diffraction (XRD) patterns were measured by a PANalytical PW3040/60X-ray powder diffractometer, using a Cu Kα irradiation source (λ = 0.15406 nm) operated at 40 kV. The time-resolved XRD patterns of ≈20 mg powder samples that have their surface wetted by water were recorded at 0, 10, 20, and 30 minutes, respectively. The transmission electron microscope (TEM, FEI Talos F200x) with an Energy Dispersive X-ray Spectrometer (EDS) was utilized to observe the morphology and microstructure of the samples. The reflectance spectra and fluorescence spectra were measured by a fiber optic spectrometer (Ocean Optics USB 2000+) with a full-spectrum white LED and a 365 nm UV lamp as the light source respectively. An X-ray photoelectron spectroscopy (XPS, Thermo K-Alpha) was used to investigate the compositions and valence states of the samples. The Raman spectra were recorded using a Thermo Fisher Scientific Raman spectrometer with a 532 nm laser. The Fourier transform infrared (FTIR) spectra were monitored on a Thermo Scientific iN10 FTIR Spectrometer. The N_2 adsorption-desorption isotherm was measured with a surface area and porosity analyzer (Micromeritics ASAP 2460).

Computational Method. First-principle calculations were performed by the density functional theory (DFT) using the Vienna Ab-initio Simulation Package (VASP) package.[44] The generalized gradient approximation (GGA) with the Perdew-Burke-Ernzerhof (PBE) functional was used to describe the electronic exchange and correlation effects.[45,46] Uniform G-centered k-points meshes with a resolution of 2π*0.05 Å^{-1} and Methfessel-Paxton electronic smearing were adopted for the integration in the Brillouin zone for geometric optimization. The simulation was run with a cutoff energy of 500 eV throughout the computations. These settings ensure convergence of the total energies to within 1 meV per atom. Structure relaxation proceeded until all forces on atoms were less than 10 meV Å^{-1} and the total stress tensor was within 0.03 GPa of the target value. A composite model was built by adsorbing a MnO_2 molecular onto the (001) surface of the $CsPbBr_3$ lattice. The surface energy of the intermediate models is calculated by the following equation:

$$\gamma_s = 1/2A * (E_{surface} - \sum \mu_i n_i) \tag{1}$$

where A represents the surface area, $E_{surface}$ is the total energy of the surface structure, and $\sum \mu_i n_i$ is the sum-up of all chemical potentials involved. Besides, n_i is the atom number of the ith element, μ_{Cs}, μ_{Mn}, and μ_{Pb} are derived from the simple substances in the conventional phase (bcc Cs and fcc Pb), and μ_{Br}, μ_O, and μ_{H_2O} are estimated from the corresponding molecules in a cubic lattice with 10 Å in dimensions. A loose k mesh of 1×1×1 was employed with criteria of 1.0×10-5 eV per atom and 0.3 eV Å^{-1}. During the relaxation, several bottom layers are frozen to simulate the surface structures.

Acknowledgements

This work was financially supported by the Guangdong Natural Science Foundation (No. 2021A1515010152), Basic and Applied Basic Research Program of Guangzhou Science and

Technology Bureau (No. 2023A03J0076), University Innovation Team Scientific Research Project of Guangzhou Education Bureau (No. 202235246).

ASSOCIATED CONTENT

Supporting Information

TEM images of the $CsPbBr_3@MnO_2$ composites prepared with the $PbBr_2$-CsBr concentration at 0.070 mmol/mL, without amino modification, or with surplus amino functional groups. XRD patterns of *h*-MnO_2 and $CsPbBr_3@MnO_2$-H. -M, and -L. XPS spectra of $CsPbBr_3$, *h*-MnO_2, and $CsPbBr_3@MnO_2$-M. SEM image of the section view of the $CsPbBr_3@MnO_2$-M film. Fluorescence response of $CsPbBr_3@MnO_2$-M film under water vapor with a flow rate at 6 L/min and different RH of 100%, 90%, 80%, and 70%. Fluorescence response of $CsPbBr_3@MnO_2$-M film under water vapor with 100% RH and different flow rates at 3 and 9 L/min. Fluorescence and reflectance spectra of $CsPbBr_3@MnO_2$-M film under static water vapor for 5 minutes. Fluorescence image of the $CsPbBr_3@MnO_2$-M nanospheres for trace water detection. Fluorescence spectra, TEM image, and response performance of $CsPbBr_{3-x}Cl_x@MnO_2$-M. TEM image of $CsPbBr_3$ nanocrystals. Surface area and porosity results of the $CsPbBr_3@MnO_2$-M nanospheres. TEM image and XRD patterns of $CsPbBr_3@MnO_2$-M after 100 cycles of water vapor treatment. Fluorescence response of the $CsPbBr_3@MnO_2$-M film stored in air for 6 months. Preparation scheme of the dual-mode information encryption patterns.

Notes

The authors declare no competing financial interest.

References

(1) Kim, J. S.; Heo, J.-M.; Park, G.-S.; Woo, S.-J.; Cho, C.; Yun, H. J.; Kim, D.-H.; Park, J.; Lee, S.-C., Park, S.-H., Yoon, E.; Greenham, N. C.; Lee, T.-W. Ultra-Bright, Efficient and Stable Perovskite Light-Emitting Diodes. *Nature* **2022**, *611*, 688–694.

(2) Hassan, Y.; Park, J. H.; Crawford, M. L.; Sadhanala, A.; Lee, J.; Sadighian, J. C.; Mosconi, E.; Shivanna, R.; Radicchi, E.; Jeong, M.; Yang, Choi, C.; Park, H.; S. H.; Song, M. H.; Angelis, D. F.; Wong, C. Friend, Y.; R. H.; Lee, B. R.; Snaith, H. J. Ligand-Engineered Bandgap Stability in Mixed-Halide Perovskite LEDs. *Nature* **2021**, *591*, 72–77.

(3) Zheng, W.; Wang, X.; Zhang, X.; Chen, B.; Suo, H.; Xing, Z.; Wang, Y.; Wei, H. L.; Chen, J.; Guo, Y.; Wang, F. Emerging Halide Perovskite Ferroelectrics. *Adv. Mater.* **2023**, *35*, 2205410.

(4) Wei, Y.; Cheng, Z.; Lin, J. An Overview on Enhancing the Stability of Lead Halide Perovskite Quantum Dots and Their Applications in Phosphor-Converted LEDs. *Chem. Soc. Rev.* **2019**, *48*, 310–350.

(5) Akkerman, Q. Rainò, A.; G.; Kovalenko, M. V.; Manna, L. Genesis, Challenges and Opportunities for Colloidal Lead Halide Perovskite Nanocrystals. *Nat. Mater.* **2018**, *17*, 394–405.

(6) Yang, D.; Li, X.; Zhou, W.; Zhang, S.; Meng, C.; Wu, Y.; Wang, Y.; Zeng, H. $CsPbBr_3$ Quantum Dots 2.0: Benzenesulfonic Acid Equivalent Ligand Awakens Complete Purification. *Adv. Mater.* **2019**, *31*, 1900767.

(7) Zhou, L.; Liao, J.-F.; Huang, Z.-G.; Wei, J.-H.; Wang, X.-D.; Li, W.-G.; Chen, H.-Y., Kuang, D.-B.; Su, C.-Y. A Highly Red-Emissive Lead-Free Indium-Based Perovskite Single Crystal for Sensitive Water Detection. *Angew. Chem. Int. Ed.* **2019**, *58*, 5277–5281.

(8) Wu, L.; Hu, H.; Xu, Y.; Jiang, S.; Chen, M.; Zhong, Q.; Yang, D.; Liu, Q.; Zhao, Y.; Sun, B.; Zhang, Q.; Yin, Y. From Nonluminescent Cs_4PbX_6 (X = Cl, Br, I) Nanocrystals to Highly Luminescent $CsPbX_3$ Nanocrystals: Water-Triggered Transformation Through a CsX-Stripping Mechanism. *Nano Lett.,* **2017,** *17*, 5799–5804.

(9) Chen, J.; Guo, Y.; Chen, B.; Zheng, W.; Wang, F. Ultrafast and Multicolor Luminescence Switching in a Lanthanide-Based Hydrochromic Perovskite. *J. Am. Chem. Soc.* **2022**, *144*, 22295–22301.

(10) Liu, Y.; Liu, G.; Wu, Y.; Cai, W.; Wang, Y.; Zhang, S.; Zeng, H.; Li, X. High-Temperature, Reversible and Robust Thermochromic Fluorescence based on $Rb_2MnBr_4(H_2O)_2$ for Anti-Counterfeiting. *Adv. Mater.* **2023**, *35*, 2301914.

(11) Liu, Z.; Bekenstein, Y.; Ye, X.; Nguyen, S. C.; Swabeck, J.; Zhang, D.; Lee, S. T.; Yang, P.; Ma, W.;

Alivisatos, A. P. Ligand Mediated Transformation of Cesium Lead Bromide Perovskite Nanocrystals to Lead Depleted Cs_4PbBr_6 Nanocrystals. *J. Am. Chem. Soc.* **2017**, *139*, 5309–5312.

(12) Li, M.; Yang, D.; Huang, X.; Zhang, H.; Zhao, Y.; Yin, B.; Pan, Q.; Kang, J.; Zheng, N.; Liu, X.; Qiu, J.; Yang, Z.; Dong, G. Coupling Localized Laser Writing and Nonlocal Recrystallization in Perovskite Crystals for Reversible Multidimensional Optical Encryption. *Adv. Mater.,* **2022**, *34*, 2201413.

(13) Kanwat, A.; Ghosh, B.; Ng, S. E.; Rana, P. J. S.; Lekina, Y.; Hooper, T. J. N.; Yantara, N.; Kovalev, M.; Chaudhary, B.; Kajal, P.; Febriansyah, B.; Tan, Q. Y.; Klein, M.; Shen, Z. X.; Ager, J. W.; Mhaisalkar, S. G.; Mathews, N. Reversible Photochromism in ⟨110⟩ Oriented Layered Halide Perovskite. *ACS Nano* **2022**, *16*, 2942–2952.

(14) Liu, S.; Sun, S.; Gan, C. K.; del Águila, A. G.; Fang, Y.; Xing, J.; Do, T. T. H.; White, T. J.; Li, H.; Huang, W.; Xiong, Q. Manipulating Efficient Light Emission in Two-Dimensional Perovskite Crystals by Pressure-Induced Anisotropic Deformation. *Sci. Adv.* **2019**, *5*, eaav9445.

(15) Chen, J.; Zeng, Y.; Sun, R.; Zhang, W.; Huang, Y.; Zheng, J.; Chi, Y. Hydrochromic Perovskite System with Reversible Blue-Green Color for Advanced Anti-Counterfeiting. *Small* **2023**, *19*, 2301010.

(16) Guan, M.; Xie, Y.; Zhang, Y.; Gu, Z.; Qiu, L.; He, Z.; Ye, B.; Suwardi, A.; Dai, Z.; Li, G.; Hu, G. Moisture-Tailored 2D Dion-Jacobson Perovskites for Reconfigurable Optoelectronics. *Adv. Mater.* **2023**, *35*, 2210611.

(17) Pi, M.; Wu, D.; Wang, J.; Chen, K.; He, J.; Yang, J.; Zhang, D.; Chen, S.; Tang, X. Real-Time and Ultrasensitive Humidity Sensor Based on Lead-Free Cs_2SnCl_6 Perovskites. *Sens. Actuators B Chem.* **2022**, *354*, 131084.

(18) Gong, Z.; Zheng, W.; Huang, P.; Cheng, X.; Zhang, W.; Zhang, M.; Han, S.; Chen, X. Highly Efficient Sb^{3+} Emitters in 0D Cesium Indium Chloride Nanocrystals with Switchable Photoluminescence through Water-Triggered Structural Transformation. *Nano Today* **2022**, *44*, 101460.

(19) Yu, X.; Wu, L.; Yang, D.; Cao, M.; Fan, X.; Lin, H.; Zhong, Q.; Xu, Y.; Zhang, Q. Hydrochromic $CsPbBr_3$ Nanocrystals for Anti-Counterfeiting. *Angew. Chem. Int. Ed.* **2020**, *59*, 14527–14532.

(20) Zhang, F.; Liang, W.; Wang, L.; Ma, Z.; Ji, X.; Wang, M.; Wang, Y.; Chen, X.; Wu, D.; Li, X.; Zhang, Y.; Shan, C.; Shi, Z. Moisture-Induced Reversible Phase Conversion of Cesium Copper Iodine Nanocrystals Enables Advanced Anti-Counterfeiting. *Adv. Funct. Mater.* **2021**, *31*, 2105771.

(21) Bian, F.; Sun, L.; Chen, H.; Wang, Y.; Wang, L.; Shang, L.; Zhao, Y. Bioinspired Perovskite Nanocrystals-Integrated Photonic Crystal Microsphere Arrays for Information Security. *Adv. Sci.* **2022**, *9*,

2105278.

(22) Wu, Z.; Du, B.; Tong, G.; Zhang, H.; Zhang, Y.; Xia, J.; Zhao, Z. Highly Luminescent and Stable Inorganic Perovskite Micro-Nanocomposites for Crucial Information Encryption and Decryption. *Chem. Eng. J.* **2022**, *428*, 131016.

(23) Chen, Y.; Zuo, Z. H.; Liu, Z. Q.; Yin, Y. Rapid Color-Switching of MnO_2 Hollow-Nanosphere Films in Dynamic Water vapor for Reversible Optical Encryption. *Small* **2022**, *18*, 2204484.

(24) Finocchio, E.; Macis, E.; Raiteri, R.; Busca, G. Adsorption of Trimethoxysilane and of 3-Mercaptopropyltrimethoxysilane on Silica and on Silicon Wafers from Vapor Phase: An IR Study. *Langmuir* **2007**, *23*, 2505–2509.

(25) Rozyyev, V.; Murphy, J. G.; Barry, E.; Mane, A. U.; Sibener, S. J.; Elam, J. W. Vapor-Phase Grafting of a Model Aminosilane Compound to Al_2O_3, ZnO, and TiO_2 Surfaces Prepared by Atomic Layer Deposition. *Appl. Surf. Sci.* **2021**, *562*, 149996.

(26) Li, X.; Wang, Y.; Sun, H.; Zeng, H. Amino-Mediated Anchoring Perovskite Quantum Dots for Stable and Low-Threshold Random Lasing. *Adv. Mater.* **2017**, *29*, 1701185.

(27) Ou, M.; Tu, W.; Yin, S.; Xing, W.; Wu, S.; Wang, H.; Wan, S.; Zhong, Q.; Xu, R. Amino-Assisted Anchoring of $CsPbBr_3$ Perovskite Quantum Dots on Porous g-C_3N_4 for Enhanced Photocatalytic CO_2 Reduction. *Angew. Chem. Int. Ed.* **2018**, *57*, 13570–13574.

(28) Zhong, C.-Y.; Li, L.; Chen, Q.; Jiang, K.-Z.; Li, F.-t.; Liu, Z.-Q.; Chen, Y. Enhanced Exciton-to-Mn^{2+} Energy Transfer in 3D/0D Cesium-Lead-Chloride Composite Perovskites. *Adv. Opt. Mater.* **2023**, *11*, 2202321.

(29) Zhong, C.-Y.; Xiao, L.; Zhou, J.; Chen, Z.; Chen, Y.; Liu, Z.-Q.; Zhang, J. Z. Two-Photon Photoluminescence and Bio-Imaging Application of Monodispersed Perovskite-in-Silica Nanocrystals with High Biocompatibility. *Chem. Eng. J.* **2022**, *431*, 134110.

(30) Wang, Z.; Huang, J.; Wang, L.; Liu, Y.; Liu, W.; Zhao, S.; Liu, Z.-Q. Cation-Tuning Induced d-Band Center Modulation on Co-Based Spinel Oxide for Oxygen Reduction/Evolution Reaction. *Angew. Chem. Int. Ed.* **2022**, *61*, 202114696.

(31) Jiang, M.; Fu, C.; Yang, J.; Liu, Q.; Zhang, J.; Sun, B. Defect-Engineered MnO_2 Enhancing Oxygen Reduction Reaction for High Performance Al-Air Batteries. *Energy Storage Mater.* **2019**, *18*, 34–42.

(32) Yan, L.; Niu, L.; Shen, C.; Zhang, Z.; Lin, J.; Shen, F.; Gong, Y.; Li, C.; Liu, X.; Xu, S. Modulating the Electronic Structure and Pseudocapacitance of δ-MnO_2 Through Transitional Metal M (M = Fe, Co and Ni) Doping. *Electrochim. Acta* **2019**, *306*, 529–540.

(33) Hong, W.; Yuan, Z.; Chen, X. Structural Color Materials for Optical Anticounterfeiting. *Small* **2020**, *16*, 1907626.

(34) Lai, X.; Ren, Q.; Vogelbacher, F.; Sha, W. E. I.; Hou, X.; Yao, X.; Song, Y.; Li, M. Bioinspired Quasi-3D Multiplexed Anti-Counterfeit Imaging via Self-Assembled and Nanoimprinted Photonic Architectures. *Adv. Mater.* **2022**, *34*, 2107243.

(35) Hou, J.; Li, M.; Song, Y. Patterned Colloidal Photonic Crystals. *Angew. Chem. Int. Ed.* **2018**, *57*, 2544–2553.

(36) Han, J. H.; Samanta, T.; Cho, H. B.; Jang, S. W.; Viswanath, N. S. M.; Kim, Y. R.; Seo, J. M.; Im, W. B., Intense Hydrochromic Photon Upconversion from Lead-Free 0D Metal Halides for Water Detection and Information Encryption. *Adv. Mater*. **2023**, *35*, 2302442.

(37) Gao, W.; Leng, M.; Hu, Z.; Li, J.; Li, D.; Liu, H.; Gao, L.; Niu, G.; Tang, J., Reversible Luminescent Humidity Chromism of Organic-Inorganic Hybrid PEA_2MnBr_4 Single Crystals. *Dalton Trans.* **2020,** *49*, 5662–5668.

(38) Shao, G.; Zhao, Y.; Yu, Y.; Yang, H.; Liu, X.; Zhang, Y.; Xiang, W.; Liang, X. Bright Emission and High Photoluminescence $CsPb_2Br_5$ NCs Encapsulated in Mesoporous Silica with Ultrahigh Stability and Excellent Optical Properties for White Light-Emitting Diodes. *J. Mater. Chem. C* **2019**, *7*, 13585–13593.

(39) Bai, L.; Xie, Z.; Wang, W.; Yuan, C.; Zhao, Y.; Mu, Z.; Zhong, Q.; Gu, Z. Bio-Inspired Vapor-Responsive Colloidal Photonic Crystal Patterns by Inkjet Printing. *ACS Nano* **2014**, *8*, 11094–11100.

(40) Wallacher, D.; Künzner, N.; Kovalev, D.; Knorr, N.; Knorr, K. Capillary Condensation in Linear Mesopores of Different Shape. *Phys. Rev. Lett.* **2004**, *92*, 195704.

(41) Zhong, K.; Li, J.; Liu, L.; Van Cleuvenbergen, S.; Song, K.; Clays, K. Instantaneous, Simple, and Reversible Revealing of Invisible Patterns Encrypted in Robust Hollow Sphere Colloidal Photonic Crystals. *Adv. Mater.* **2018**, *30*, 1707246.

(42) Ge, J.; Yin, Y. Responsive Photonic Crystals. *Angew. Chem. Int. Ed.* **2011**, *50*, 1492–1522.

(43) Zhao, H.; Lin, T.; Shi, S.; Bai, W.; Xuan, T.; Zhou, T.; Xie, R.-J. Water-Induced Reversible Phase Transformation between Cesium Lead Halide Perovskite Nanocrystals Enables Fluorescent Anti-Counterfeiting. *J. Mater. Chem. C* **2022**, *10*, 7552–7557.

(44) Kresse, G.; Furthmuller, J. Efficiency of ab-initio Total Energy Calculations for Metals and Semiconductors Using a Plane-Wave Basis Set. *Comput. Mater. Sci.* **1996**, *6*, 15–50.

(45) Perdew, J. P.; Burke, K.; Ernzerhof, M. Generalized Gradient Approximation Made Simple. *Phys. Rev. Lett.* **1996**, *77*, 3865–3868.

(46) Kresse, G.; Joubert, D. From Ultrasoft Pseudopotentials to the Projector Augmented-Wave Method. *Phys. Rev. B* **1999**, *59*, 1758–1775.

For Table of Contents Only

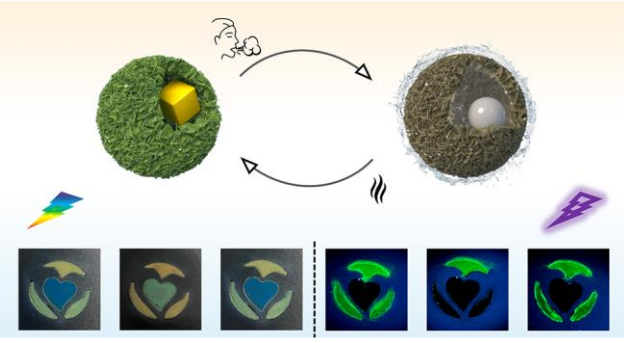

Supporting Information

Designing Yolk-Shell Nanostructures for Reversible Water-Vapor-Responsive Dual-Mode Switching of Fluorescence and Structural Color

Zhi-Han Zuo[a], Zi-Wen Feng[a], Ying-Ying Peng[a], Yucong Su[d], Zhao-Qing Liu[a], Guogang Li[b,c], Yadong Yin[d], and Yibo Chen[a*]*

[a] *School of Chemistry and Chemical Engineering/Institute of Clean Energy and Materials/Key Laboratory for Clean Energy and Materials, Guangzhou University, Guangzhou Higher Education Mega Center, No. 230 Wai Huan Xi Road, 510006, P. R. China*

[b] *Faculty of Materials Science and Chemistry, China University of Geosciences, Wuhan, Hubei 430074, P. R. China*

[c] *Zhejiang Institute, China University of Geosciences, Hangzhou, Zhejiang 311305, P. R. China*

[d] *Department of Chemistry, University of California Riverside, CA 92521, USA*

**Corresponding authors: Guogang Li, E-mail: ggli@cug.edu.cn; Yibo Chen, E-mail: chenyibo@gzhu.edu.cn.*

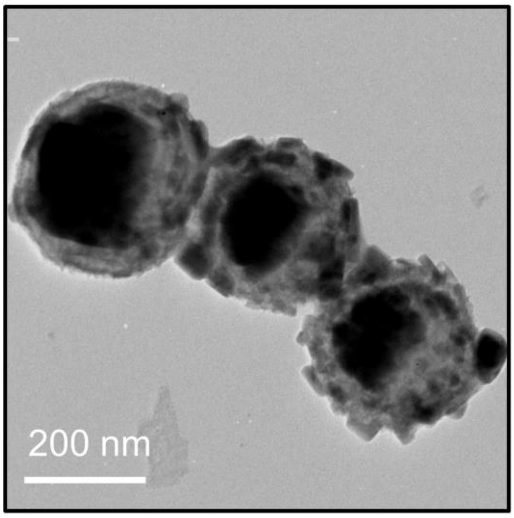

Figure S1. TEM image of the $CsPbBr_3@MnO_2$ composite prepared with the $PbBr_2$-CsBr concentration at 0.014 mmol/mL.

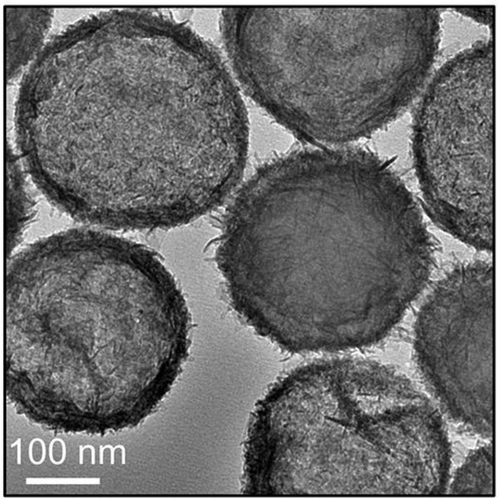

Figure S2. TEM image of the $CsPbBr_3@MnO_2$ composite prepared without amino modification.

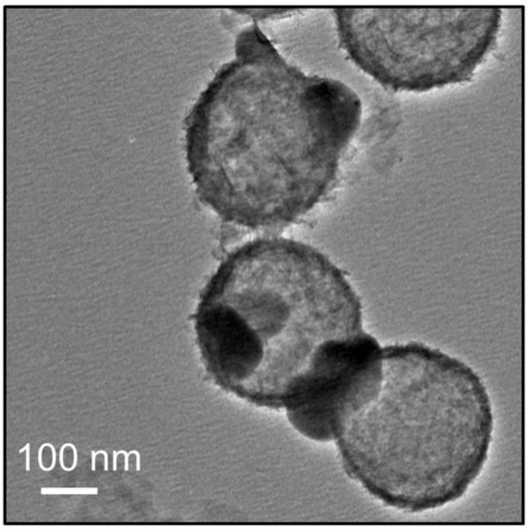

Figure S3. TEM image of the $CsPbBr_3@MnO_2$ composite prepared with surplus amino functional groups.

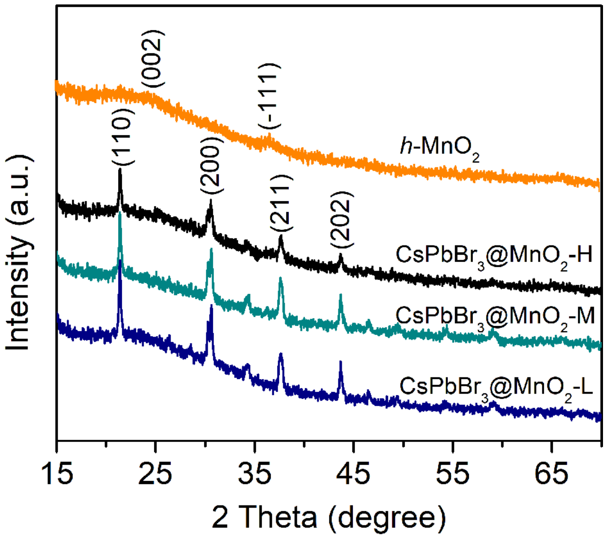

Figure S4. XRD patterns of *h*-MnO_2 and $CsPbBr_3@MnO_2$-H. -M, and -L.

The diffraction patterns of *h*-MnO_2 show two broad peaks at 24.6° and 36.7°, corresponding to the (002) and (−111) crystal planes of birnessite-type manganese oxide (JCPDS card No. 80-1098).[1] The diffraction peaks of $CsPbBr_3@MnO_2$ composites are mainly presented at 21.5°, 30.7°, 37.6°, and 43.7°, which are consistent with the characteristic (110), (200), (211), and (202) crystal planes of $CsPbBr_3$ (JCPDS card No.18-0364).[2] The diffraction peaks of *h*-MnO_2 are not detectable in the composite because of the low crystallinity.

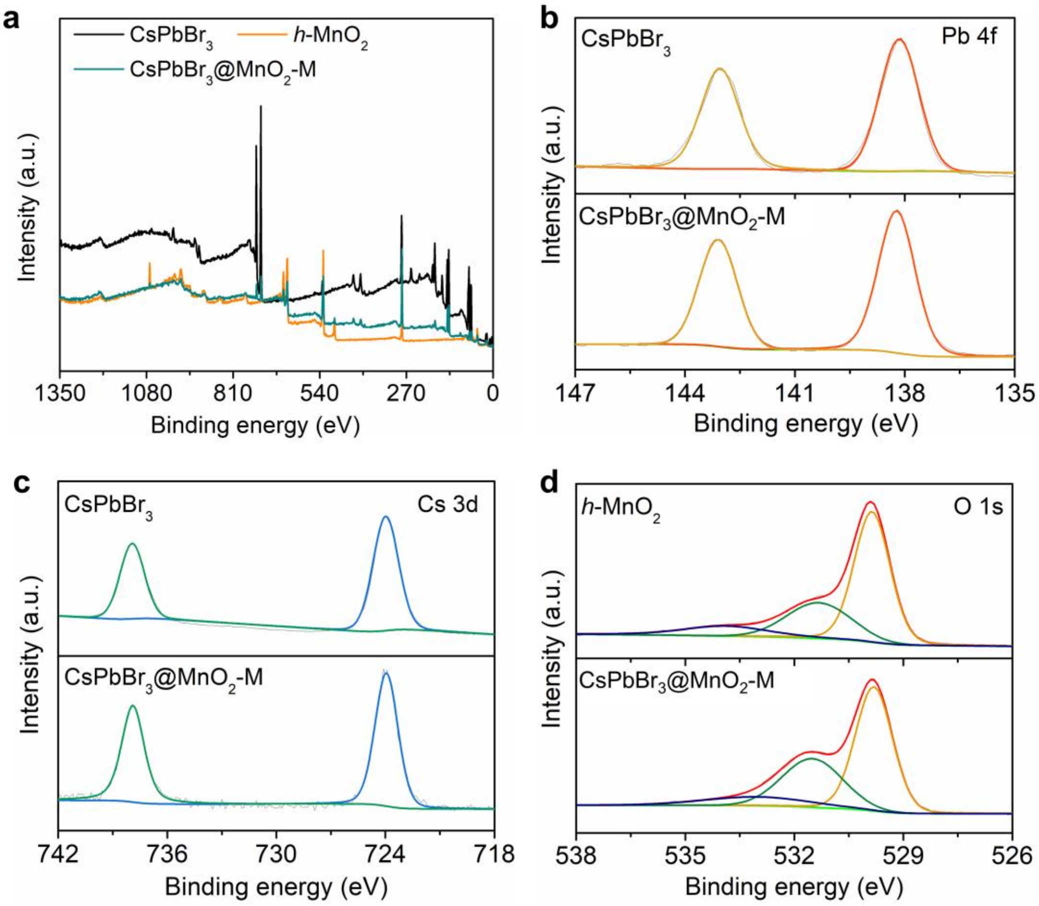

Figure S5. XPS spectra of CsPbBr$_3$, *h*-MnO$_2$, and CsPbBr$_3$@MnO$_2$-M. (a) Survey spectra. (b) High-resolution XPS spectra of Pb 4f. (c) High-resolution XPS spectra of Cs 3d. (d) High-resolution XPS spectra of O 1s.

The Pb 4f$_{5/2}$ and Pb 4f$_{7/2}$ peaks of the CsPbBr$_3$ nanocrystals locate at 138.15 and 143.05 eV.[3] The binding energy of Pb 4f$_{7/2}$ in CsPbBr$_3$@MnO$_2$-M shifts 0.07 eV towards higher values compared with the CsPbBr$_3$ nanocrystals. The two peaks of Cs 3d$_{3/2}$ and Cs 3d$_{5/2}$ of CsPbBr$_3$ are located at 723.97 and 737.95 eV.[3] No significant shift is observed in Cs 3d spectrum of CsPbBr$_3$@MnO$_2$-M compared with single-phase CsPbBr$_3$. The H-O-H bond at 533.9 eV in O 1s orbital of CsPbBr$_3$@MnO$_2$-M shifts to a lower binding energy compared with *h*-MnO$_2$, and the Mn-O-H bond at 531.7 eV shifts to a higher binding energy.[4] These changes are due to the electronic structure alteration of Mn.

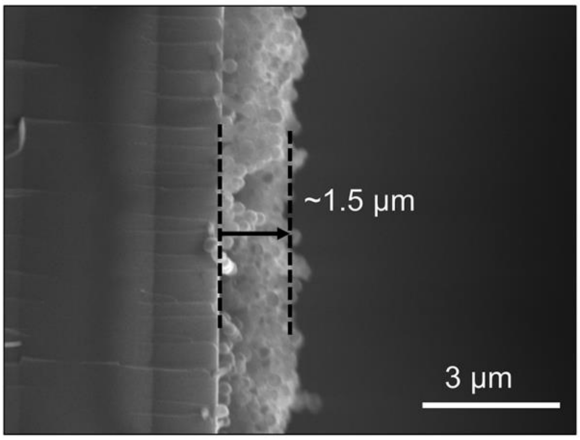

Figure S6. SEM image of the cross-section view of the $CsPbBr_3@MnO_2$-M film.

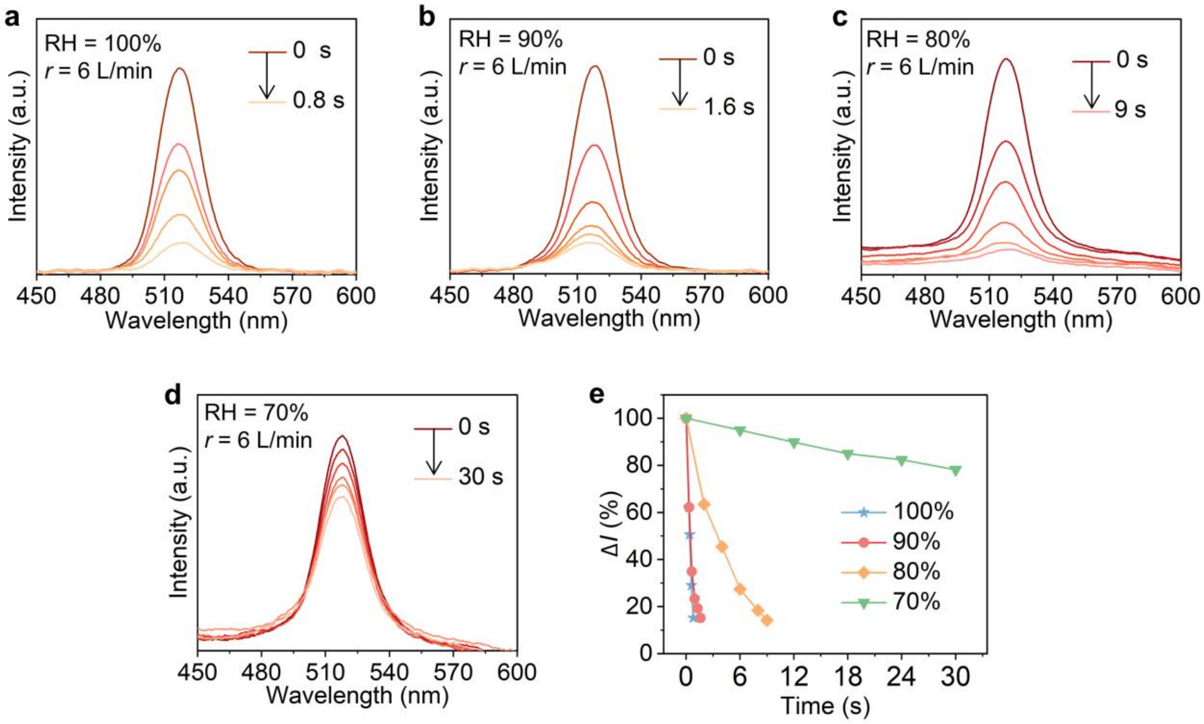

Figure S7. Fluorescence spectra of $CsPbBr_3@MnO_2$-M film under water vapor with the flow rate at 6 L/min and different RH of (a) 100%, (b) 90%, (c) 80%, (d) 70%. (e) Comparison of the response time.

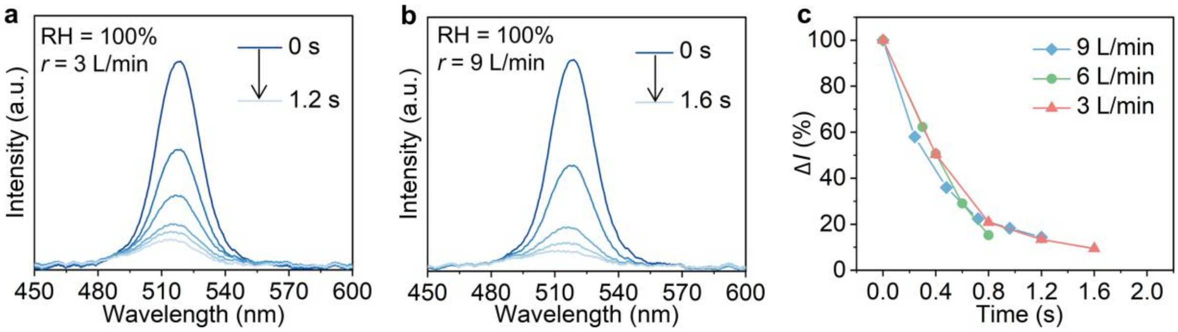

Figure S8. Fluorescence spectra of $CsPbBr_3@MnO_2$-M film under water vapor with 100% RH and different flow rate at (a) 3 L/min, and (b) 9 L/min. (c) Comparison of the response time. All data in Figure S7 and Figure S8 is monitored using one single film.

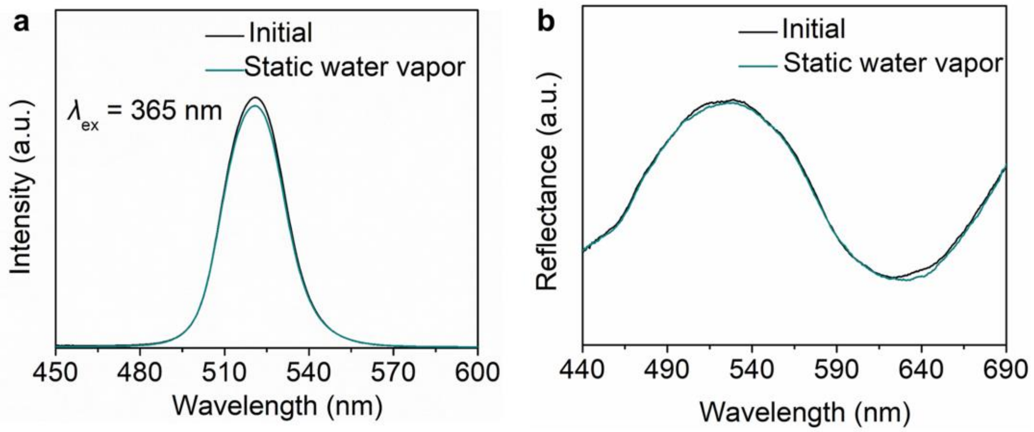

Figure S9. (a) Fluorescence and (b) reflectance spectra of $CsPbBr_3@MnO_2$-M film under static water vapor (r = 0 L/min) for 5 minutes.

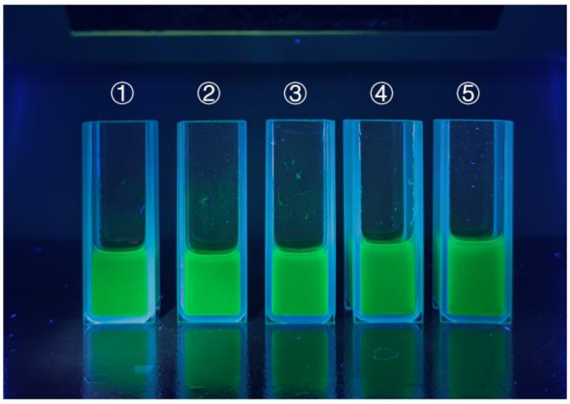

Figure S10. Fluorescence image of the $CsPbBr_3@MnO_2$-M nanospheres dispersed in tetrahydrofuran (THF) solution. The addition amount of water in 2.0 mL THF is 0, 0.5, 1.0, 2.0, and 20.0 µL for ①, ②, ③, ④, and ⑤, respectively.

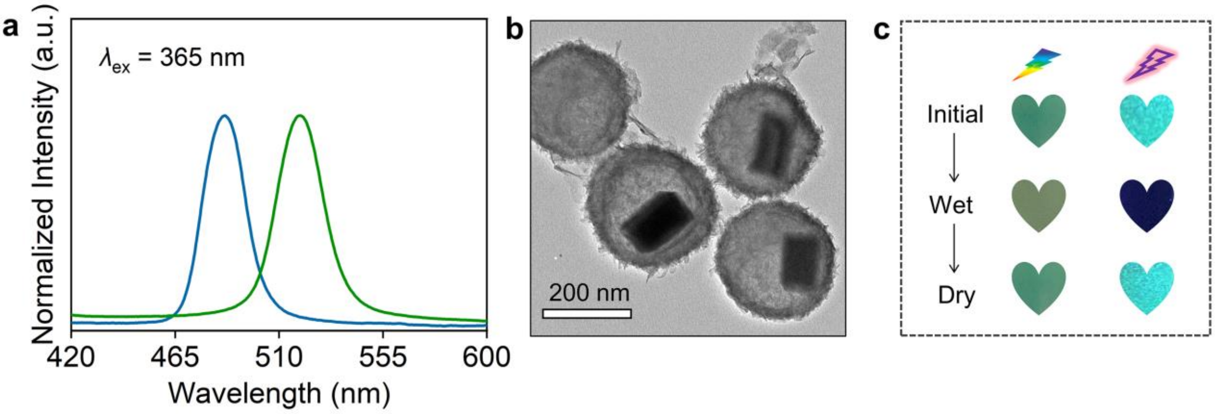

Figure S11. (a) Fluorescence spectra of $CsPbBr_{3-x}Cl_x@MnO_2$-M (blue line) and $CsPbBr_3@MnO_2$-M (green line). (b) TEM image of the $CsPbBr_{3-x}Cl_x@MnO_2$-M nanospheres. (c) Photos of the $CsPbBr_{3-x}Cl_x@MnO_2$-M film under dynamic water vapor.

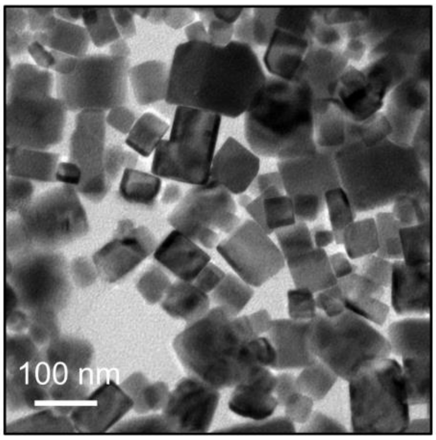

Figure S12. TEM image of $CsPbBr_3$ nanocrystals.

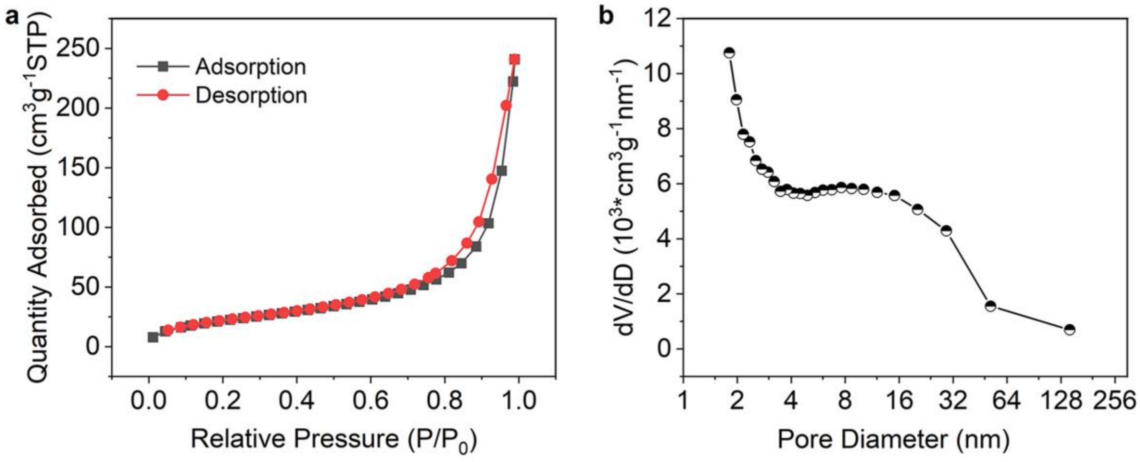

Figure S13. Surface area and porosity results. (a) Nitrogen adsorption-desorption isotherm, and (b) pore size distribution of the $CsPbBr_3@MnO_2$-M nanospheres. The BET surface area is 83.66 m^2g^{-1} and the average pore diameter derived by BTH model is 16.86 nm.

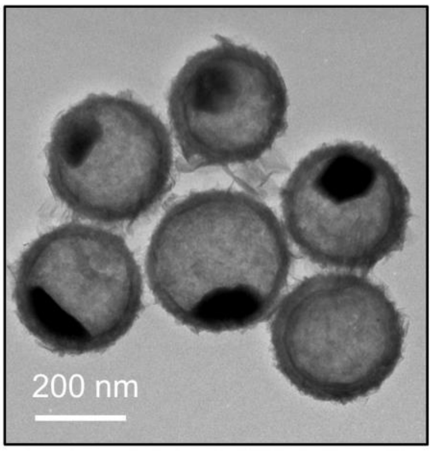

Figure S14. TEM image of $CsPbBr_3@MnO_2$-M after 100 cycles of water vapor treatment.

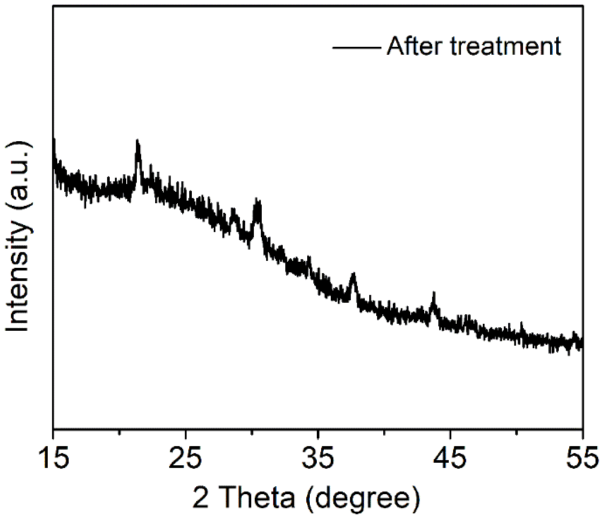

Figure S15. XRD patterns of $CsPbBr_3@MnO_2$-M after 100 cycles of water vapor treatment.

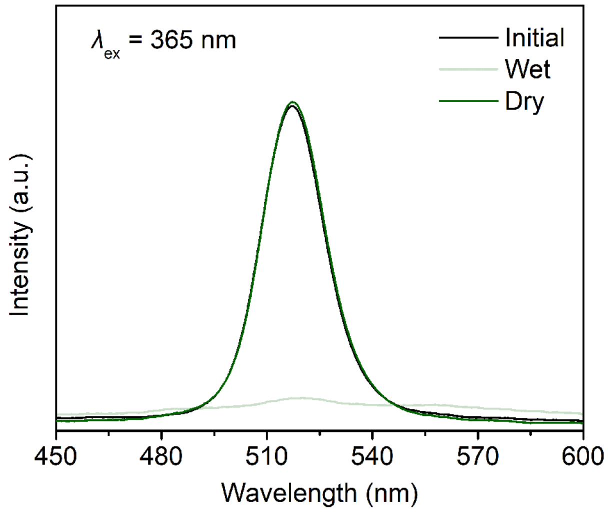

Figure S16. Fluorescence response of the $CsPbBr_3@MnO_2$-M film which has been stored in air for 6 months. The dynamic water vapor used for stimulus is at 100% RH and a flow rate of 6 L/min.

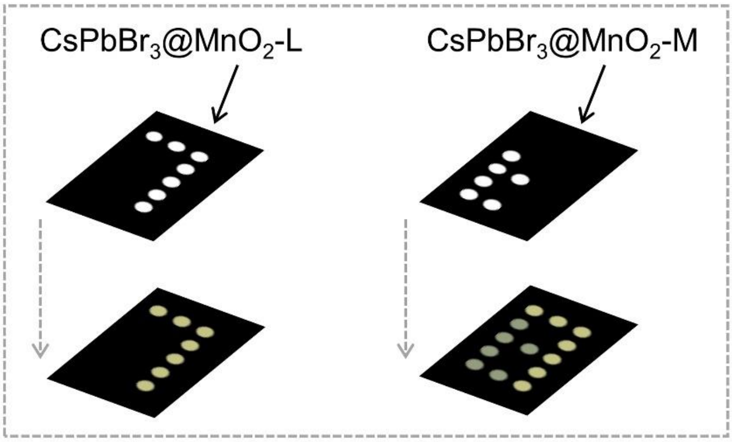

Figure S17. Preparation scheme of the dual-mode information encryption patterns.

Table S1. Crystal parameters for a specific [$PbBr_6$] octahedron with or without bonding MnO_2.

Samples	Bond length (Å)	Bond angle (°)	Distortion index
Bare $CsPbBr_3$	2.980	92.417	0.009
$CsPbBr_3$ with MnO_2	3.295	98.250	0.239

The distortion index ($\overline{D}$) could be calculated by using the following equation:[5]

$$\overline{D} = \frac{1}{n}\sum_{i=1}^{n}\left(\frac{|d_i - d_{av}|}{d_{av}}\right) \qquad (1)$$

where n is the coordination number of the center cation, d_i and d_{av} are the distance and average distance between the Pb and Br atoms.

Table S2. Response features of the previous water/moisture-responsive reported metal halides.

Materials	Stimulus type	Response mode	Repetition numbers	Ref.
$CsPbBr_3$@MnO_2-M	High-humidity dynamic water vapor	Both in fluorescence and structural color	100	This work
$Cs_3TbF_6{:}Eu^{3+}$	Water/moisture	Fluorescence	20	[6]
$CsPbBr_3$@MSNs	Moisture	Fluorescence	10	[7]
$(C_6H_{18}N_2O_2)PbCl_4{:}Mn^{2+}$	Moisture	Fluorescence	10	[8]
$Cs_2InBr_5 \cdot H_2O$	Trace water/moisture	Fluorescence	20	[9]
$Cs_3Cu_2I_5$	Moisture	Fluorescence	10	[10]
$Cd^{2+}{:}CsPbX_3$@MSHSs	Water	Fluorescence	20	[11]
Cs_4PbX_6 NCs	Trace water/moisture	Fluorescence	20	[12]
$Cs_3GdCl_6{:}Yb^{3+},Er^{3+}$	Trace water/moisture	Fluorescence	15	[13]

References

(1) Bai, Y. C.; Yao, X. X.; Wang, X. J.; Yin, Y. D. Surface-Initiated Redox Route to Hollow MnO_2 Nanostructures. *ChemNanoMat* **2020**, *6*, 1186–1190.

(2) Kim, H.; Bae, S.-R.; Lee, T. H.; Lee, H.; Kang, H.; Park, S.; Jang, H. W.; Kim, S. Y. Enhanced Optical Properties and Stability of $CsPbBr_3$ Nanocrystals Through Nickel Doping. *Adv. Funct. Mater.* **2021**, *31*, 2102770.

(3) Zhong, C.-Y.; Xiao, L.; Zhou, J.; Chen, Z.; Chen, Y.; Liu, Z.-Q.; Zhang, J. Z. Two-Photon Photoluminescence and Bio-Imaging Application of Monodispersed Perovskite-in-Silica Nanocrystals with High Biocompatibility. *Chem. Eng. J.* **2022,** *431*, 134110.

(4) Yang, W.; Su, Z. a.; Xu, Z.; Yang, W.; Peng, Y.; Li, J. Comparative Study of α-, β-, γ- and δ-MnO_2 on Toluene Oxidation: Oxygen Vacancies and Rreaction Intermediates. *Appl. Catal. B* **2020,** *260*, 118150.

(5) Lin, F.; Li, X.; Chen, C.; Pan, X.; Peng, D.; Luo, H.; Jin, L.; Zhuang, Y.; Xie, R.-J. Modeling Polyhedron Distortion for Mechanoluminescence in Mixed-Anion Compounds $Re_2O_2S:Ln^{3+}$. *Chem. Mater.* **2022**, *34*, 5311–5319.

(6) Chen, J.; Guo, Y.; Chen, B.; Zheng, W.; Wang, F. Ultrafast and Multicolor Luminescence Switching in a Lanthanide-Based Hydrochromic Perovskite. *J. Am. Chem. Soc.* **2022**, *144*, 22295–22301.

(7) Yu, X.; Wu, L.; Yang, D.; Cao, M.; Fan, X.; Lin, H.; Zhong, Q.; Xu, Y.; Zhang, Q. Hydrochromic $CsPbBr_3$ Nanocrystals for Anti-Counterfeiting. *Angew. Chem. Int. Ed.* **2020**, *59*, 14527–14532..

(8) Guan, M.; Xie, Y.; Zhang, Y.; Gu, Z.; Qiu, L.; He, Z.; Ye, B.; Suwardi, A.; Dai, Z.; Li, G.; Hu, G. Moisture-Tailored 2D Dion-Jacobson Perovskites for Reconfigurable Optoelectronics. *Adv. Mater.* **2023**, *35*, 2210611.

(9) Zhou, L.; Liao, J.-F.; Huang, Z.-G.; Wei, J.-H.; Wang, X.-D.; Li, W.-G.; Chen, H.-Y., Kuang, D.-B.; Su, C.-Y. A Highly Red-Emissive Lead-Free Indium-Based Perovskite Single Crystal for Sensitive Water Detection. *Angew. Chem. Int. Ed.,* **2019**, *58*, 5277–5281.

(10) Zhang, F.; Liang, W.; Wang, L.; Ma, Z.; Ji, X.; Wang, M.; Wang, Y.; Chen, X.; Wu, D.; Li, X.; Zhang, Y.; Shan, C.; Shi, Z. Moisture-Induced Reversible Phase Conversion of Cesium Copper Iodine Nanocrystals Enables Advanced Anti-Counterfeiting. *Adv. Funct. Mater.* **2021**, *31*, 2105771.

(11) Wu, Z.; Du, B.; Tong, G.; Zhang, H.; Zhang, Y.; Xia, J.; Zhao, Z. Highly Luminescent and Stable Inorganic Perovskite Micro-Nanocomposites for Crucial Information Encryption and Decryption. *Chem. Eng. J.* **2022**, *428*, 131016.

(12) Zhao, H.; Lin, T.; Shi, S.; Bai, W.; Xuan, T.; Zhou, T.; Xie, R.-J. Water-Induced Reversible Phase Transformation between Cesium Lead Halide Perovskite Nanocrystals Enables Fluorescent Anti-Counterfeiting. *J. Mater. Chem. C* **2022**, *10*, 7552–7557.

(13) Han, J. H.; Samanta, T.; Cho, H. B.; Jang, S. W.; Viswanath, N. S. M.; Kim, Y. R.; Seo, J. M.; Im, W. B., Intense Hydrochromic Photon Upconversion from Lead-Free 0D Metal Halides For Water Detection and Information Encryption. *Adv. Mater*. **2023**, *35*, 2302442.